

For Reference

NOT TO BE TAKEN FROM THIS ROOM

Ex libris
UNIVERSITATIS
ALBERTAEASIS





Digitized by the Internet Archive
in 2020 with funding from
University of Alberta Libraries

<https://archive.org/details/Burch1971>

127
29
THE UNIVERSITY OF ALBERTA

LOW ENERGY ION BOMBARDMENT OF STAINLESS STEEL

by



WILLIAM GEORGE BURCH

A THESIS

SUBMITTED TO THE FACULTY OF GRADUATE STUDIES
IN PARTIAL FULFILMENT OF THE REQUIREMENTS FOR THE DEGREE
OF MASTER OF SCIENCE IN
ELECTRICAL ENGINEERING

DEPARTMENT OF ELECTRICAL ENGINEERING

EDMONTON, ALBERTA

FALL, 1971

UNIVERSITY OF ALBERTA

FACULTY OF GRADUATE STUDIES

The undersigned certify that they have read, and recommend to the Faculty of Graduate Studies for acceptance, a thesis entitled "LOW ENERGY ION BOMBARDMENT OF STAINLESS STEEL" submitted by William George Burch in partial fulfilment of the requirements for the degree of Master of Science in Electrical Engineering.

Date ..30th June 1971.....

ABSTRACT

A vacuum system and associated electronic apparatus has been assembled to study surface properties of metals and semiconductors.

The observations reported in this work are the result of bombarding stainless steel with 75 eV to 500 eV helium ions and studying the post-bombardment thermal re-emission of trapped gas. The observations generally agree with published work in correlating desorption spectra with migration energies. The observed diffusion activation energy, however, agrees with published values for α -Fe rather than γ -Fe.

ACKNOWLEDGEMENTS

The author wishes to thank his supervising professor, Dr. R.P.W. Lawson, for his understanding of the problems involved and encouragement given during the course of this research.

The technical staff, in particular the machine shop personnel, with the Department of Electrical Engineering are to be praised for their co-operation and high quality of workmanship.

In addition, the personnel with the Ministry of Transport must be thanked for their co-operation and assistance in the completion of this thesis.

The financial support provided by the Department of Electrical Engineering is gratefully acknowledged.

TABLE OF CONTENTS

	Page
CHAPTER 1 INTRODUCTION	1
CHAPTER 2 BOMBARDMENT OF SOLIDS	
2.1 Lattice Defects	3
2.2 Collision Kinetics	5
2.3 Many-Body Effects	6
CHAPTER 3 ANNEALING AND GAS KINETICS	
3.1 Thermal Desorption	9
3.2 Characteristics of Desorption Spectra	12
3.3 Gas Location	13
CHAPTER 4 APPARATUS AND PROCEDURE	
4.1 Chamber Construction	16
4.2 Gas-Handling Plant	22
4.3 Chamber Calibration	23
4.4 Ion Beam Generator	28
4.5 Sample Configurations	32
4.6 Specimen Heating Rate	33
4.7 Detection of Desorbed Gas	33
4.8 Operating Procedure	35
CHAPTER 5 EXPERIMENTAL RESULTS AND DISCUSSION	
5.1 Introduction	40
5.2 Experimental Results	41
5.3 Interpretation of Results	51
CHAPTER 6 CONCLUSION	61
BIBLIOGRAPHY	63

LIST OF FIGURES

	Page
FIGURE 2.1 An Edge Dislocation	4
2.2 A Screw Dislocation	4
2.3 Channelling	4
FIGURE 3.1 Release Mechanisms in Nickel	15
FIGURE 4.1 Chamber Layout	17
4.1 Sect a-a'	18
4.1 Sect b-b'	19
4.2 Vacuum System Block Diagram	20
4.3 Gas Handling Plant	21
4.4 Pumping Speed	25
4.5 Leak Valve Conductance	26
4.6 Calibration Curves for Mass Spectrometer	27
4.7 Ion Beam Generator Electrode Configuration	30
4.8 Typical Ion Beam Energy Curves	31
4.9 Specimen Temperature Versus Time	34
4.10 Operational Block Diagram	37
4.11 High Impedance Operational Amplifier	38
4.12 Differentiator Schematic	39
FIGURE 5.1 Results from Argon Desorption	42
5.2 Results from Helium Desorption	42
5.3 Argon Desorption Constant Dose 2×10^{14} Ions/cm ²	43
5.4 Helium Desorption Constant Dose 1×10^{14} Ions/cm ²	44
5.5 Helium Desorption Constant Dose 1×10^{14} Ions/cm ²	45
5.6 Helium Desorption Constant Dose 2×10^{14} Ions/cm ²	46
5.7 Helium Desorption Constant Dose 2×10^{14} Ions/cm ²	47

FIGURE 5.8	Helium Desorption Constant Dose 2×10^{14} Ions/cm ²	48
5.9	Helium Desorption Constant Energy 200 eV	49
5.10	Helium Desorption Constant Energy 200 eV	50
5.11	Log ($n_0 T_p^2$) Versus $\frac{1}{T_p}$	52
5.12a	Desorption Rate as a Function of Dose (Linear)	58
5.12b	Desorption Rate as a Function of Dose (Linear)	59
5.13	Desorption Rate as a Function of Dose (Logarithmic)	60

LIST OF SYMBOLS

α -iron	bcc iron
γ -iron	fcc iron
ϵ	coefficient of secondary electron emission
E_T	maximum energy transfer (eV)
E_I	incident energy (eV)
A	sample area (cm ²)
N(t)	desorption rate (molecules/cm ² /sec)
V	volume
S	pumping speed
K	3.27×10^{19} molecules/liter
τ	time constant $\frac{V}{S}$
n	number of atoms
ν	rate constant (10^{13} sec ⁻¹)
x	order of a reaction
E	activation energy (eV)
R	Boltzman constant
T	temperature
t	time
b	heating rate
T ₀	initial temperature
T _p	temperature at which a desorption peak occurs
α_1	first desorption peak
α_2	second desorption peak
η	third desorption peak
β	fourth desorption peak
G.H.P.	gas-handling plant
P	pressure
P _u	ultimate pressure

V_{RX}	reference volume
Q	gas throughput (liter/sec)
k	calibration factor
C	conductance

CHAPTER 1

INTRODUCTION

In the last decade, considerable interest has developed in the use of ion beams with carefully controlled energy and dose rate to study physical properties of materials or changes in properties due to ion bombardment. Physical properties of metals can be examined in both the damaged and undamaged state by choice of the bombarding energy. The field of surface science has become especially important with the use of semiconductors in outer space, where they may be irradiated by dust particles, gas molecules or electromagnetic radiation. Ion implantation is being studied for manufacture of semiconductors. Using ion implantation, the usual diffusion doping limits can be exceeded and ions can be injected into a relatively cold crystal. It has been found that this method allows more accurate monitoring of the number of ions implanted and precise control of the depth profile, with facilities for completely programmed control of the ion beam. Care must be taken to ensure that the ions are directed along open channel directions to minimize damage caused by bombardment of the crystal. The annealing process necessary to relieve the stresses created during ion penetration must be done without desorbing the implanted ions. Considerable study of ion implantation and annealing mechanisms is necessary for successful manufacture of semiconductors using this method.

It can be seen that a versatile system capable of bombarding either bulk materials or thin films can obtain information of value to metallurgists, surface scientists and production or manufacturing engineers. To be of most use, a certain degree of versatility and flexibility must be built into the system. It should be capable of studying either solid targets such as metal plate and ribbon or thin

metallic or semiconductor films with only minor modifications necessary to change specimens. In addition, several different parameters may be measured with each type of specimen. Solid specimens reveal surface parameters such as work function, trapping efficiency, annealing kinetics and gas profiles. Thin films, by virtue of their shallow depth, may be used to study bulk effects such as resistivity and minority carrier lifetime, in addition to surface effects. In order to obtain truly representative surface parameters, obtaining and maintaining a surface free of gas contamination places definite pressure requirements on the system.

The work to be presented describes the construction of an ultra-high vacuum system and ion beam generator, together with associated control and measuring equipment. Observations obtained with the system will be given which demonstrate some of its capabilities.

CHAPTER 2

BOMBARDMENT OF SOLIDS2.1 Lattice Defects

A knowledge of basic lattice defects is necessary before the effects of an energetic ion entering a surface can be fully appreciated.

The most simple imperfection is a missing atom, or vacancy, known as a Schottky defect. Atoms in non-normal positions are interstitials. If the vacancy has been produced by the interstitial, then the defect is known as a Frenkel pair. It has been shown that vacancies and interstitials tend to aggregate.^{1,2} Combinations of vacancies result in a lower stored energy because of the smaller surface to volume ratio. Interstitials tend to form clusters because the force between them tends to be attractive at distances prevalent in solid lattices at thermal energies.

There are also several types of line defects known as dislocations. An edge dislocation, see Fig 2.1, is the boundary between a stationary plane of atoms and a plane in which part of the atoms have slipped sideways by one lattice distance. A screw dislocation, shown in Fig 2.2, transforms successive atom planes into the surface of a helix. A dislocation can never end within a crystal; it must form a closed loop or extend to the surface. Two or more dislocations can interact with one another, and they generally absorb vacancies and interstitials. Burgers⁴ has suggested that low-angle grain boundaries consist of arrays of dislocations.

The thermal energy of the atoms makes possible a continuous creation and destruction of these defects. Huntington and Seitz⁵ suggested three possible mechanisms for defect migration in copper. These are:

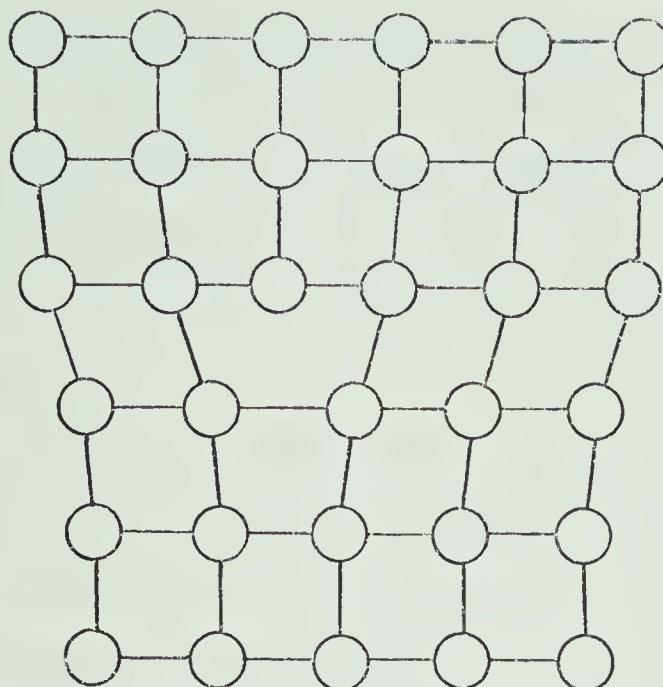


FIGURE 2.1 AN EDGE DISLOCATION

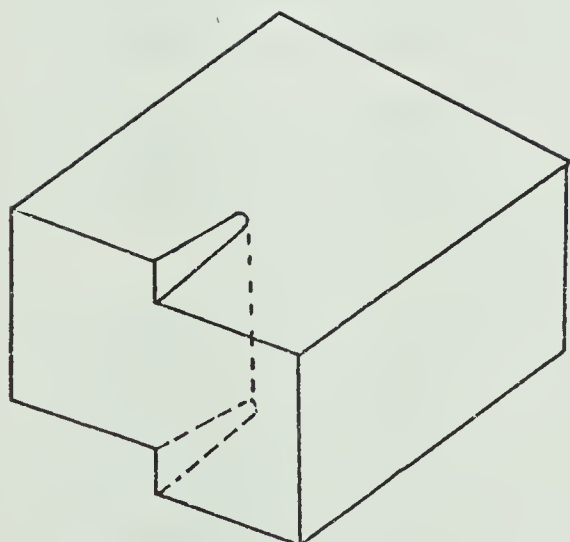


FIGURE 2.2 A SCREW DISLOCATION

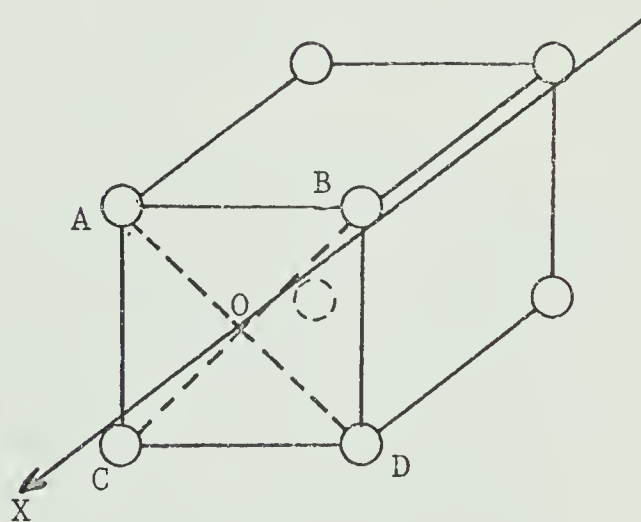


FIGURE 2.3 CHANNELLING

- 1) direct interchange of two adjacent lattice atoms,
- 2) migration of a lattice atom into an adjacent vacancy,
- 3) an interstitial displaces a nearest neighbour, the latter becoming an interstitial in the next plane.

Grain boundaries and dislocations offer relatively little resistance to diffusion of atoms.

The above defect structures can be normally present within a crystalline lattice at concentrations dependent upon the crystallization process. The manufacture of any material by extrusion, cold rolling or drawing and quenching will also introduce such defects and the properties of the solid structure so formed may be determined by the defect type and concentration.

Ion bombardment is often used to introduce defects and to study defect properties. To fully understand these processes, a knowledge of basic bombardment kinetics is necessary.

2.2 Collision Kinetics

As an ion approaches a surface, several events may occur. On approaching the surface, it will be neutralized and may liberate electrons or ions from the surface; it may be reflected or it may penetrate the surface. Electron secondary emission and the events following ion penetration are of interest here.

Electron secondary emission is of interest because an electron leaving is identical to an ion arriving as far as a current detector is concerned. A coefficient ϵ is defined as the number of electrons emitted per incident ion. Although no known values of ϵ for stainless steel have been found, a value of $\epsilon = 0.26$ will be used. This approximates the value given for tungsten with helium ions over an energy range of 100 eV to 1,000 eV. Coefficients of ion emission are generally small and corrections to recorded ion currents from secondary ion emission can be ignored. ⁷

The description of penetration of ions at the low energies used in this work becomes complex because the ion interacts with more than one atom at a time. Factors which influence the interaction of moving particles in a lattice are their mass, energy and charge. When the primary ion has an energy of several hundred KeV, inelastic collisions dominate, and the major energy loss is due to electronic excitation and ionization. As the primary slows down, elastic collisions transfer kinetic energy to the lattice atoms which, if not used to displace the atom, must be dissipated as heat or phonons. The primary now begins to interact with several lattice atoms at a time. Since low energy ions are used in this work, it is sufficient to consider only two-body kinetics and the basic equation for maximum energy transfer,

$$E_T = E_I \frac{4m_1m_2}{(m_1+m_2)^2}$$

One normally assumes that when the primary energy is degraded to about 25 eV, it becomes trapped either as a substitutional lattice atom or an interstitial. Previously trapped primaries will affect the trajectory of incoming particles by being in non-normal positions or differing in size from a normal lattice atom.

2.3 Many-Body Effects

During ion bombardment, many different ion paths are followed, and it can be shown how some of these paths lead to extremely long primary ranges. A simple cubic structure can be used to illustrate an effect called channelling. Consider the plane ABCD, Fig 2.3, with an atom at each corner and an axis X, perpendicular to and running through the centre of the plane. The net force on a primary at O will be zero, but if it should deviate from the OX axis, the net force acting on the displaced atom will tend to return it to the centre of the plane. The force on the primary along the OX

axis fluctuates periodically with X , but is always directed along the OX axis. Once started along OX , this becomes the only direction a primary may travel in order to lose energy. Distances travelled will be large because primary and lattice atom separation will be large. Little energy transfer will take place as opposed to head-on collisions in a random trajectory.

The primary energy may be transferred for long distances by focussed collisions. If the first in a line of atoms is struck head-on, the impulse may be transferred along the row of atoms. From collision kinetics, it is known that the hard sphere radius increases with decreasing energy. Hence successive collisions occur with a progressively larger radius and, if the initial collision angle is small, then subsequent collisions occur at progressively smaller angles.

As the primary slows down to several hundred eV, displacement events are no longer widely separated. Violent, localized damage occurs as many lattice atoms move away from the extended centre of the region. Since the secondary energy is small, they are trapped close to the extended centre, forming a vacancy rich region surrounded by interstitials. An energetic primary can give enough energy to a series of secondaries along its path such that each secondary creates these displacements. Volume damage like this is called a displacement spike.

As mentioned earlier, an atom becomes trapped with an energy of 25 eV or less. This excess energy of about 25 eV is dissipated by non-displacement collisions at a characteristic frequency of about 10^{13} to 10^{14} c/s. The neighbour atoms' increase in energy is equivalent to raising their temperature to over 1000° K. The energy is dissipated by normal conduction processes in approximately 10^{-11} seconds.

With a basic knowledge of the structure of solids and some types of defects that can be produced by ion bombardment, it can now be shown that by observing controlled annealing rates, theories of defect type and location may be formed.

CHAPTER 3

ANNEALING AND GAS KINETICS3.1 Thermal Desorption

In the previous section, the basic types of defect configurations and their production were described. A technique frequently used to study the trapping mechanism and location of injected ions is post-bombardment heating of the target. Heating causes escape from the trapping configuration, migration to the surface and effusion from the target. By observing the release rate as a function of temperature, an activation energy can be deduced and assigned to annealing processes mentioned earlier. The release rate can be obtained from the pumping equation

$$AN(t) + KSP_{eq} = KSP + KV \frac{dP}{dt} \quad (1)$$

where A is the sample area (cm^2)

N is the desorption rate ($\text{molecules/cm}^2/\text{sec}$)

V is the volume of the system (litres)

S is the pumping speed (l/sec)

and $K = 3.27 \times 10^{19}$ molecules/litre

at $P = 1$ torr

and $T = 295^\circ \text{K}$

By putting $P^* = P - P_{eq}$

$$\text{then } \frac{dP^*}{dt} + \frac{P^*}{\tau} = aN(t) \quad (2)$$

where $a = \frac{A}{KV}$

and $\tau = \frac{V}{S}$

For large values of τ

$$N(t) \approx \frac{dP^*}{dt} \quad (3)$$

Since inert gases are to be used, adsorption may be neglected and very large values of τ may be used. Alternatively, τ can be very small and $N(t)$ can be expressed as a function of pressure, but this was not done because of the difficulty in obtaining the same speed, S , for all experiments. Using $S = 0$, an electronic differentiator was used to observe $N(t)$.

Desorption may also be expressed by the general Arrhenius equation for rate processes,

$$\frac{dn}{dt} = -n^x v_x e^{-E/RT} \quad (4)$$

where x is the order of the reaction

v is the rate constant (10^{13} sec^{-1})

E is the activation energy (cal/mole)

For first order desorption, the rate equation is

$$\frac{dn}{dt} = -nv_1 e^{-E/RT} \quad (5)$$

A plot of $\ln \left(\frac{dn}{dt} \right)$ against $\frac{1}{RT}$ should be linear with a slope E and the intercept on the $\frac{1}{RT}$ axis will be nv . However, using a linear temperature relationship $T = T_0 + bt$, Redhead⁹ shows that

$$\frac{E}{RT_p} = \ln \left(\frac{v_1 T_p}{b} \right) - 3.64$$

and from Fig 3 of his paper, one can see that $E \approx 60 T_p$ (T in 1000° K) when b takes values between 20° K/sec and 50° K/sec

and $E \approx 67 T_p$ for $b = 1^\circ \text{ K/sec}$

In order to calculate the initial site population n_0 , the rate equation, (4), may be integrated to yield

$$\frac{dni}{dt} \approx \frac{n_0 b E}{RT_p^2 e} \quad (6)$$

Carter¹⁰ shows that the temperature at maximum release rate is given by

$$T_p = - \frac{E}{R} \frac{1}{\log \left(- \frac{bE}{Rv_0} \right)} \quad (7)$$

One may note that, for first order reactions, the temperature at maximum rate is independent of the initial dose but the maximum rate itself is linearly dependent on the initial population and the desorption energy. The temperature at maximum rate is an approximately logarithmic function of the heating rate, while the maximum rate is a linear function of b .

For a second order reaction, the rate equation is

$$\frac{dn}{dt} = -v_2 n^2 e^{-E/RT} \quad (8)$$

It can be shown ^{9,10} that T_p now depends on n_0 , the initial surface coverage. A first order reaction for which the activation energy is coverage dependent will also show a variation in T_p for differing surface coverage. However, if $\log(n_0 T_p^2)$ is plotted against $\frac{1}{T_p}$, the second order reaction with fixed activation energy yields a straight line.

If the order (x) of a reaction is unknown for the equation

$$\frac{dn}{dt} = -v_x n^x e^{-E/RT}$$

a plot of

$$\frac{n \frac{d^2n}{dt^2}}{(\frac{dn}{dt})^2} \text{ against } \frac{n}{RT^2} \frac{\frac{dT}{dt}}{\frac{dn}{dt}}$$

has a slope E , and the intercept is the order of the reaction.

Redhead ⁹ derives equations for the shape of the curve from which the order of the reaction can be determined and whether the activation energy is constant or a function of surface coverage. Of interest are the equations describing the shape of the curve about the peak.

For a first order reaction

$$\ln \left(\frac{N_p}{N} \right) = \frac{E}{R} \left(\frac{1}{T} - \frac{1}{T_p} \right) + \left(\frac{T}{T_p} \right)^2 \exp \left\{ -\frac{E}{R} \left(\frac{1}{T} - \frac{1}{T_p} \right) \right\} - 1 \quad (9)$$

and for a second order reaction

$$\frac{N}{N_p} = \frac{1}{4} \left\{ \exp \left(-\frac{E}{R} \left(\frac{1}{T_p} - \frac{1}{T} \right) \right) + \left(\frac{T}{T_p} \right)^2 \exp \left(-\frac{E}{2R} \left(\frac{1}{T} - \frac{1}{T_p} \right) \right) \right\}^2 \quad (10)$$

$$\approx \cosh^2 \left(-\frac{E}{2R} \left(\frac{1}{T} - \frac{1}{T_p} \right) \right)$$

when $\left(\frac{T}{T_p} \right)^2 \rightarrow 1$

It is apparent that the first order curve is asymmetric while the second order curve is symmetric about the maximum.

If a peak is clearly distinguished from other peaks, the difference in symmetries is sufficient to determine the order of the reaction by visual examination.

3.2 Characteristics of Desorption Spectra

The previous section derived desorption curve parameters for a linearly increasing temperature. Certain features are characteristic of desorption spectra regardless of the temperature function used. Four to ten distinct lower energy peaks, referred to as α -peaks, are present and generally a broader high temperature peak (the β peak) is found. The α peaks are independent of ion energy and increase linearly with dose. The β peak appears at ion energies above 300 eV to 400 eV, and is found to shift upwards in temperature with increasing ion energy and dose. Kornelsen¹¹ found that β peak temperatures were highest for close-packed crystal directions in which the depth of penetration will be greatest. The β peak amplitude increases almost linearly for doses up to at least $3 \times 10^{15}/\text{cm}^2$. From the work of the previous section, it is apparent that α peaks represent first order reactions and β peaks are from second order reactions. There is an element of uncertainty in analysing results because gas release may pertain to a different trapping configuration than that in which the ion came to rest since intermediate stages of annealing may occur as the solid is heated.

Kelly ¹² suggested gas release may be in three stages. In stage I, gas close to the surface is released. This involves energy of vacancy migration and is determined by damage configurations or surface proximity. This is the dominant process for low-energy bombardment. Higher bombarding energies result in deeper penetration. Gas release occurs after a normal diffusion process, and this stage (II) requires a higher temperature for gas release. A third process occurs after large ion doses from which gas bubbles are able to form, and the gas is released due to bubble migration.

Although it was believed that α peaks were gas released in a single activated step from sites within 10\AA of the surface, desorption theory shows that the peak widths are far too wide. Kornelson ¹³ found that peaks are shifted from 460°K for a (110) crystal to 540°K for a (211) crystal. From these results, it is inferred that the peak width for a polycrystalline target is due to a smearing of many different crystal faces and the peak is an indication of the most probable activation energy.

3.3 Gas Location

The location of gas and trapping configuration in the metal will be related to bombarding ion species and incident energy, total dose and the atomic structure of the target itself. However, studies show little variation for different gases, indicating that desorption spectra are characteristic of the target. In addition to sites produced by bombardment, an ill-defined target contains defect-rich areas such as grain-boundaries, dislocations, cracks and surface irregularities. Kornelson ¹⁴ found 99% of the gas trapped in tungsten after 400 eV xenon bombardment was within 10\AA ($\pm 2\text{\AA}$) of the surface. From this, he concluded that the sites are all within three lattice constants of the surface. He also found that for increasing doses

of neon, the α peaks were shifted to higher temperatures, while for krypton, the shift was to lower temperatures. For neon he suggested that knock-on collisions drove previously trapped neon deeper, while the increased stopping power of the surface layer of krypton atoms prevented deep penetration. For higher incident energies, surface effects become less important.

Not all of the defects produced will be observed. Defects such as close-Frenkel pairs separated by up to 10 lattice spacings have been shown ¹⁵ to recombine spontaneously. The life-time of an interstitial as deep as $100A^0$ with a migration energy of 0.1 eV has been shown ¹⁶ to be about 10^{-8} seconds before it is lost to the para-surface.

Most of the trapped gas, therefore, resides within the para-surface; hence, principally surface effects are observed. Surface migration of atoms along different planes can account for several α peaks. Motion of the vacancy allows release of entrapped gas immediately below the surface. Bayly ¹⁷ believes that the effect of grain boundaries is negligible in comparison to depth damage if the crystallite diameters are greater than $1000A^0$. However, grain boundaries can account for gas release even at ambient temperatures, and Barnes ¹⁸ has observed bubble formation at grain boundaries and dislocation loops. On heating the target, vacancies are produced at grain boundaries and the free surface, and migrate to agglomerate with trapped gas to precipitate bubbles. Migration of these bubbles because of the temperature gradient results in release of bursts of gas at the target surface. The lower strain field surrounding a cluster has been found ¹⁹ to capture vacancies and interstitials up to 30 and 160 atomic spacings, respectively, in copper. Vacancy and interstitial clusters form in planar fashion, causing dislocation loops in these planes.

In general, one can say that in the range 0.1 eV to 1.5 eV, migration of interstitials dominates, and from 1.5 eV to 2.0 eV, migration of vacancies begins. Bulk diffusion energies are higher. Typical is that for helium in tungsten; formation plus migration of a vacancy requires 5.23 ± 0.2 eV. An assignment of activation energies to physical processes by Rantanen et al ²⁰ is given in Table 3.1.

Release Mechanism	Activation Energy
Interstitial Migration	1.03 eV to 1.09 eV
Vacancy Migration	1.55 eV
Vacancy Formation	1.35 eV
Surface Diffusion	1.68 eV
Nickel Self-Diffusion	2.65 eV to 2.83 eV
Helium Self-Diffusion	

FIGURE 3.1 Release Mechanisms in Nickel

CHAPTER 4

APPARATUS AND PROCEDURE4.1 Chamber Construction

In chapter one, it was specified that the background pressure must be kept low to prevent contamination of the specimen. If a nominal working time of one hour is set as the monolayer formation time, then a pressure less than 1×10^{-9} torr becomes necessary. For a small working factor, the system was designed for pressures of 1×10^{-10} torr.

The pressure requirement necessitated a bakeable stainless steel experimental chamber. A four foot by three foot marinite deck supported the floor of the bake-out oven. The chamber was made of type 304 stainless steel six inches in diameter by twelve inches long. In order to have the versatility outlined in chapter one, ports using Conflat flanges were symmetrically placed on two planes, shown as cross-sections a-a' and b-b' in Fig 4.1. The six inch port, see section a-a', was designed specifically for a window, and the 2 3/4 inch port opposite it housed the ion beam generator. This arrangement allowed precise alignment of the ion beam generator with a specimen mounted from any port in plane a-a', or in the end port. Ports not used at present will be needed for thin-film experiments for which at least two evaporators and masks are used. Plane b-b' was used to mount semi-permanent components such as the pressure gauge, an NRC-563-K Bayard-Alpert ion gauge, a titanium sublimation pump and a Varian leak valve. The end port, in conjunction with a cross, positioned the mass spectrometer out of line-of-sight with the specimen. The chamber was connected to a 2 1/2 inch right angle valve.

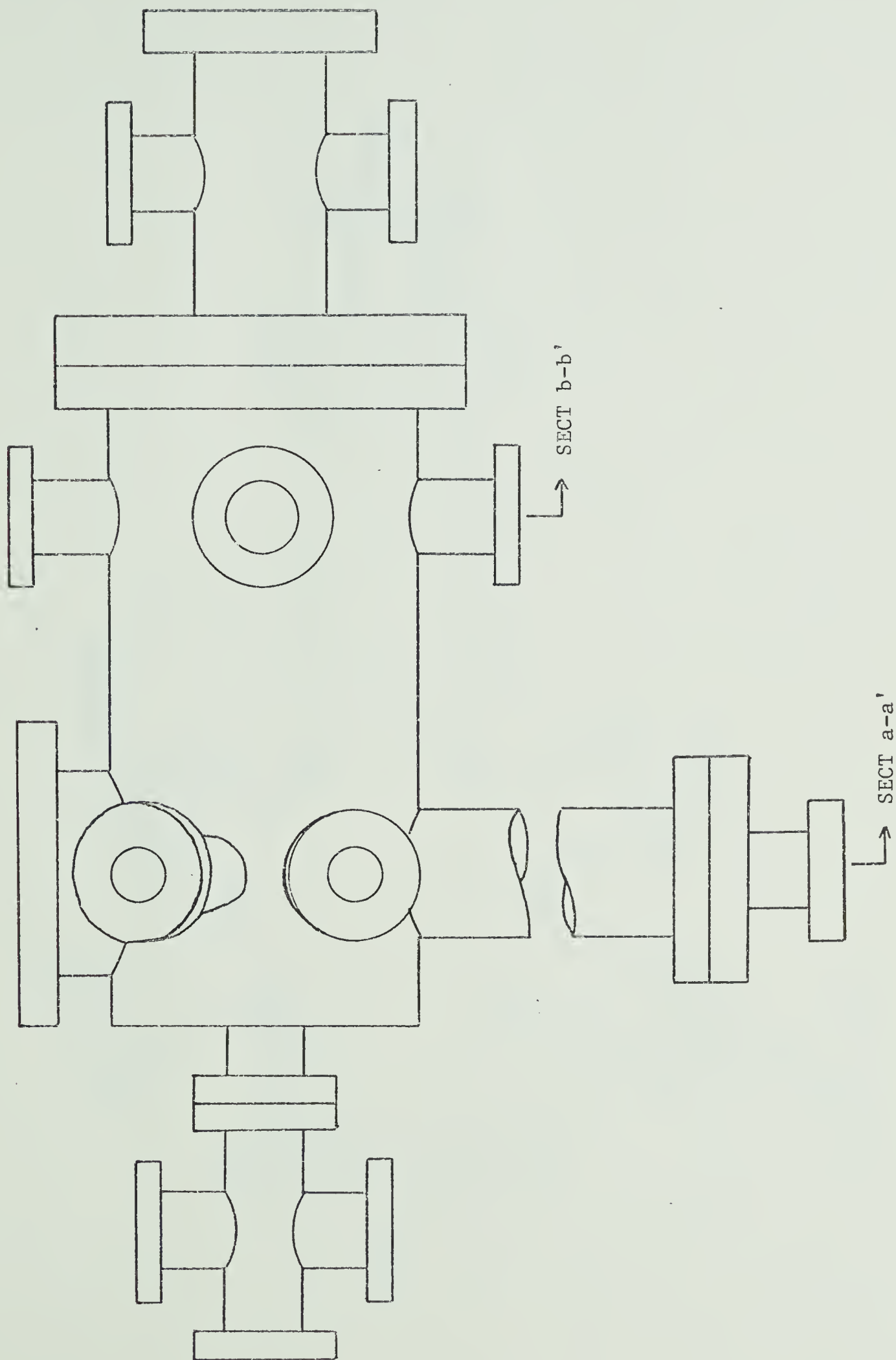


FIGURE 4.1 CHAMBER LAYOUT

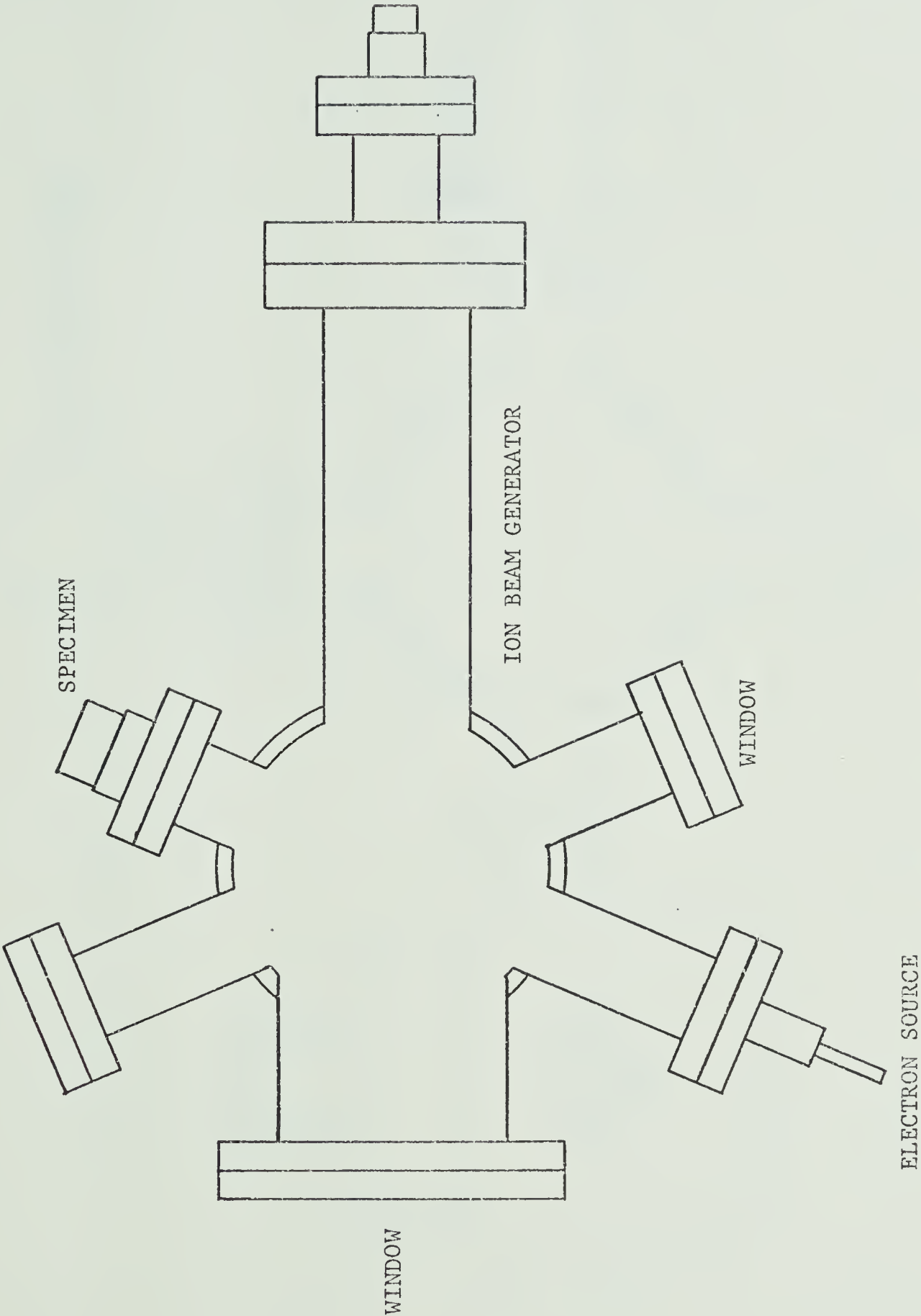


FIGURE 4.1 SECT a-a'

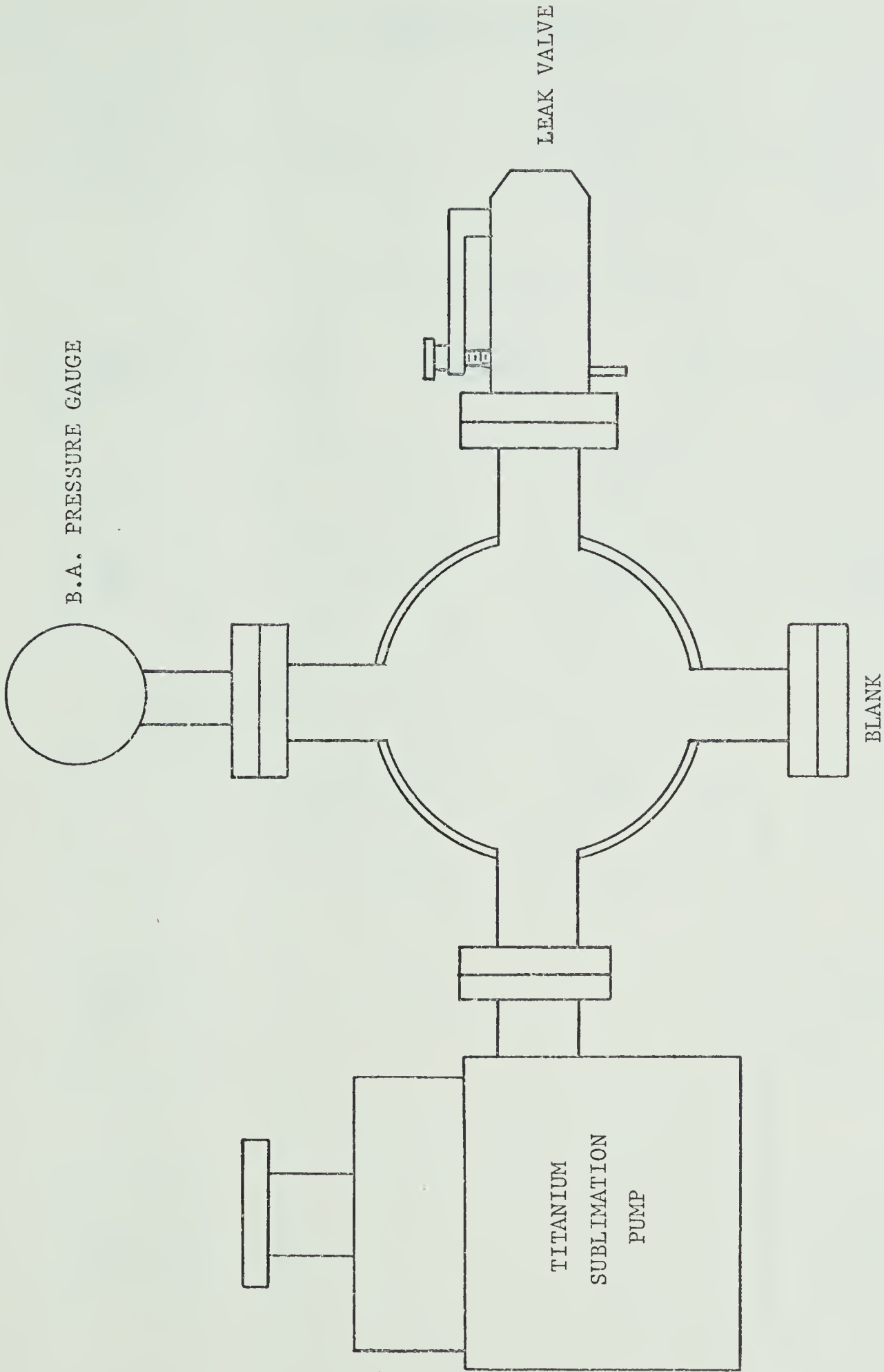
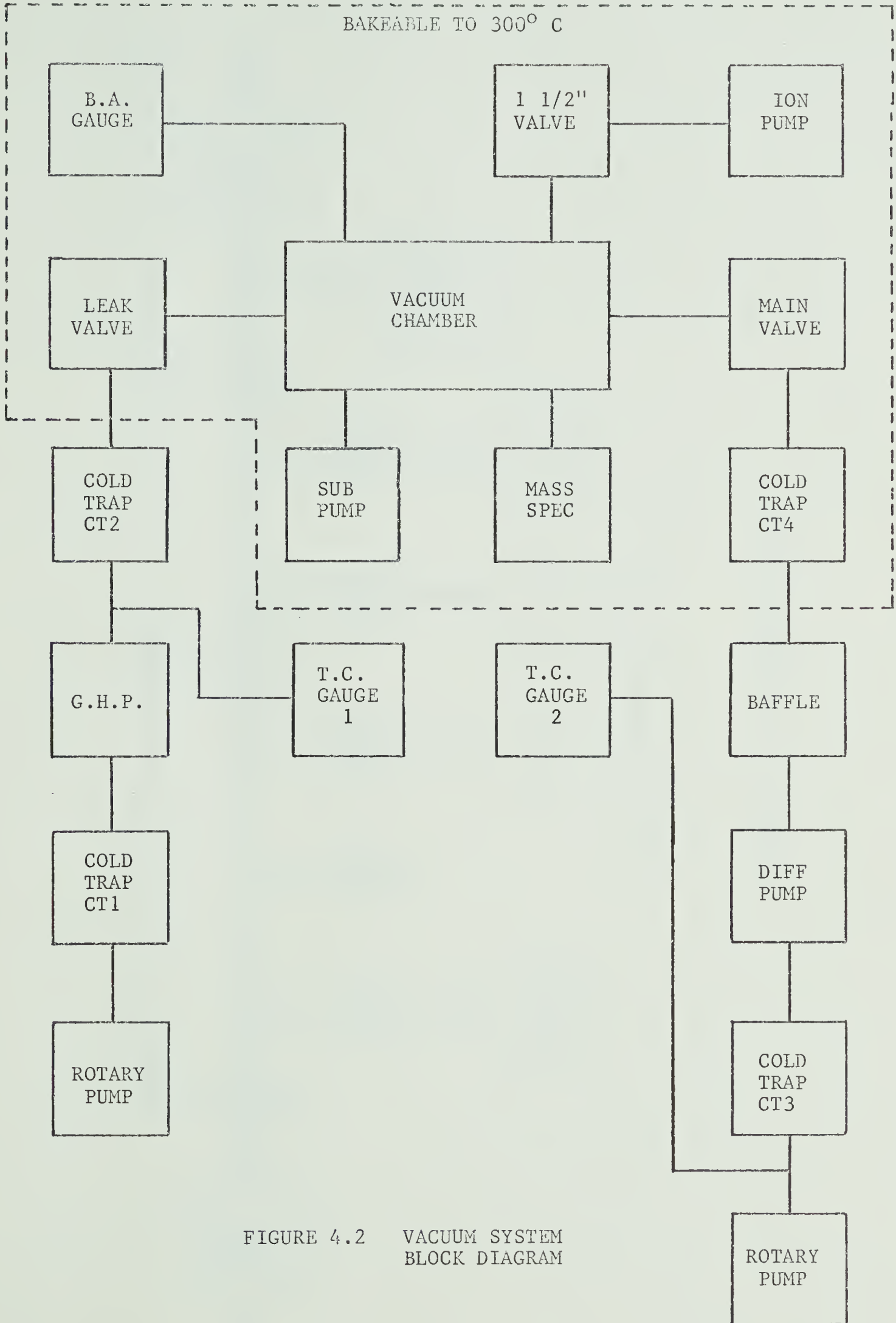
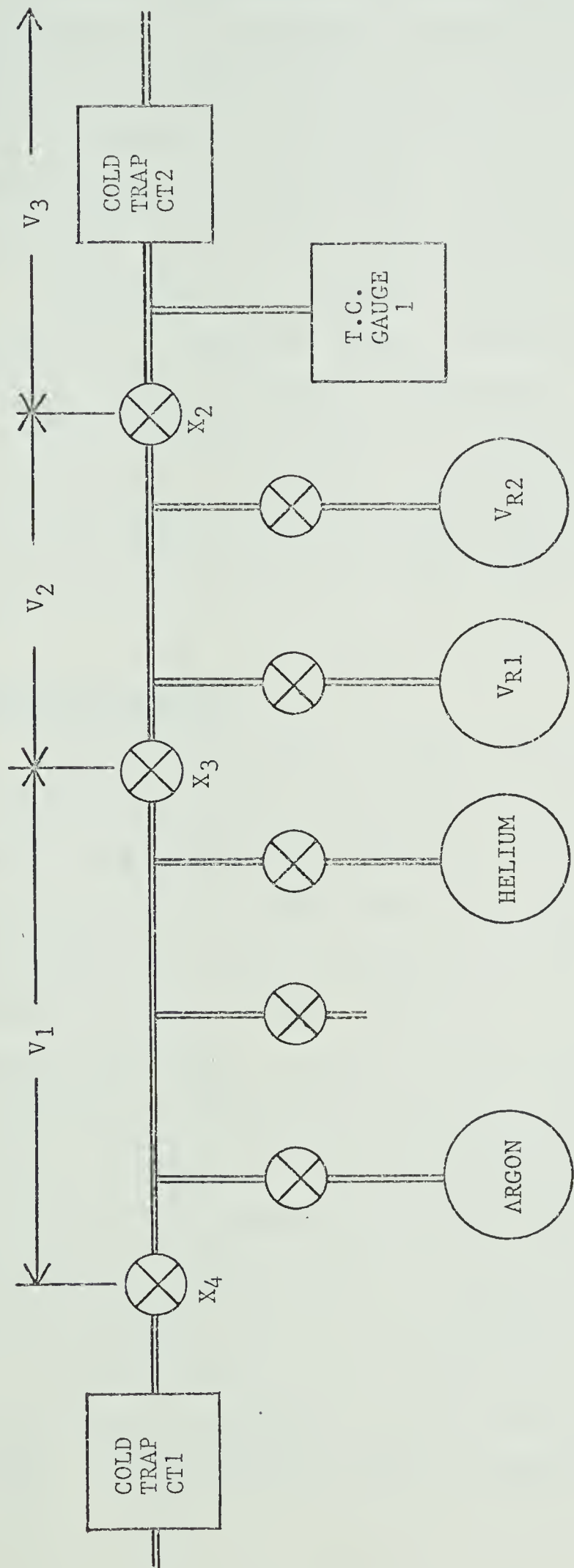


FIGURE 4.1 SECT b-b'





ALL VALVES SHOWN ARE NUPRO B-4H

FIGURE 4.3 GAS HANDLING PLANT

The main pumping system consisted of a vertically aligned two inch pumping stack comprising an Edwards NTM2A cold trap with CBA2 cold baffle and an EO2 diffusion pump. Dow-Corning DC-705 oil was used for its low vapour pressure and because it is a relatively safe oil should the hot pump accidentally be exposed to air. A liquid nitrogen trapped Edwards ED75 rotary pump backed the diffusion pump.

In addition, a 15 liter/sec Varian 'Vac-Ion' pump was used to maintain U.H.V. conditions during extended periods of unattended use, but was valved off during the experiments.

If the chamber was going to be isolated for more than about five minutes during an experiment, the titanium sublimation pump was cycled to selectively pump active gases such as H_2 , N_2 , CO , CO_2 , O_2 and H_2O .

4.2 Gas-Handling Plant

A gas-handling plant or G.H.P. is essential for calibration of the experimental chamber and for rapid cycling of bombardment experiments. This was a non-bakeable system which operates at about 10^{-3} torr, pumped by an Edwards ED35 rotary pump. Panel mounted on the deck support for ease of operation and accessibility for routine replacement of the gas bottles, the G.H.P. was made of 0.25 inch O.D. hard-drawn copper tubing. Tubing-to-tubing connections were made with soft-soldered tees, while Swagelok connectors were used with Nupro B-4H valves. The G.H.P. pressure was monitored on the thermocouple section of the NRC 763 gauge control unit. Gases used were obtained from Union Carbide, Linde Division in one liter glass bottles and were guaranteed to contain less than seven parts per million impurities.

It was necessary to accurately determine volume V_3 , see Fig 4.2, so that the ion gauge and mass spectrometer could be calibrated. A reference volume V_{R1} was established before mounting on

the G.H.P. by finding the weight of water contained in that volume. A corrected density of 0.9978 gm/cc (at 22° C) was used for water. After calibration of the thermocouple gauge with a Vacustat, a pressure P_1 was set up in volume V_3 . Volume V_2 was then pumped down to a pressure P_u . When valve X_2 was opened, a new pressure P_2 was found. Then by Boyle's Law,

$$V_2 P_u + V_3 P_1 = (V_2 + V_3) P_2.$$

Defining the ratio $a = \frac{V_3}{V_2}$

$$\text{then } a = \frac{P_2 - P_u}{P_1 - P_2}$$

This procedure was repeated, beginning with a pressure P_1 in reference volume V_{R1} which was then combined with volume $(V_2 + V_3)$. Then $V_{R1} P_1 + (V_2 + V_3) P_u = (V_{R1} + V_2 + V_3) P_2$

$$V_2 + V_3 = V_{R1} \left(\frac{P_1 - P_2}{P_2 - P_u} \right)$$

But since $V_2 = \frac{V_3}{a}$

$$\text{Then } V_3 = V_{R1} \left(\frac{a}{1+a} \right) \left(\frac{P_1 - P_2}{P_2 - P_u} \right)$$

The average value found was $V_3 = 75.1$ cc. Using a similar procedure, the volume of the main vacuum chamber was found to be 8.85 liters.

4.3 Chamber Calibration

With the G.H.P. calibrated and the volume of the main chamber known, it was then possible to calibrate the mass spectrometer and ion gauge for helium. The effective pumping speed was found by recording the pressure and time as the system was pumped down from an indicated pressure of 1×10^{-5} torr on the ion gauge. Using the basic equation

$$Q - S_e P_s = V \frac{dP_s}{dt}$$

it can be assumed that the calibration factor will be constant, so that

$$P_3 = kP_g$$

where P_s is the actual pressure

k is the calibration factor

P_g is the indicated pressure.

If no gas enters the system through leaks, then

$$S_e k P_g = - V \frac{dkP_g}{dt}$$

$$\text{So } \ln P_g \Big|_{P_1}^{P_2} = - \frac{S_e}{V} t \Big|_{t_1}^{t_2}$$

Thus, a graph of $\ln P_g$ against time has a slope $- S_e/V$.

Keeping the same pumping speed, the leak valve was opened slightly and the pressure decrease in volume V_3 was recorded. Using $S = 0$ in the G.H.P., but with a loss of helium through the leak valve, the pumping equation is:

$$Q - SP = V \frac{dP}{dt}$$

$$Q = - C (P_{GHP} - P_s) = V \frac{dP_{GHP}}{dt}.$$

But $P_{GHP} \gg P_s$

$$\text{So that } \frac{dP_{GHP}}{P_{GHP}} = - \frac{C}{V} dt$$

Now, a plot of ' $\ln P_{GHP}$ against time' yields the conductance of the leak valve. If equilibrium values of P_{GHP} , P_g and P_{ms} are recorded, a calibration factor may then be calculated for the ion gauge and mass spectrometer. This follows from the pumping equation

$$Q - SP = V \frac{dP}{dt}$$

Under equilibrium conditions $\frac{dP}{dt} = 0$.

Then $Q = -C(P_{GHP} - P_s) = S_e P_s$

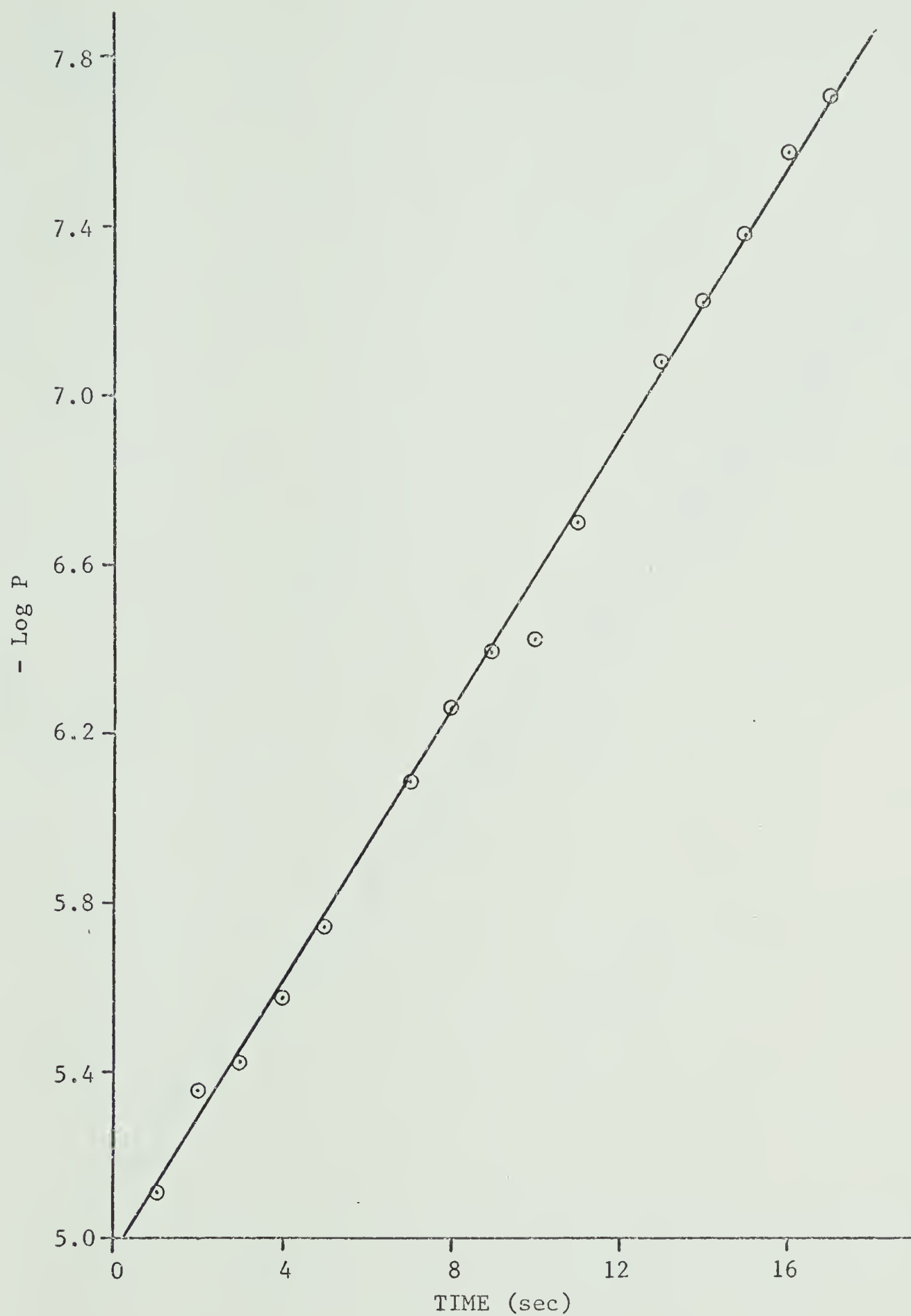


FIGURE 4.4 PUMPING SPEED

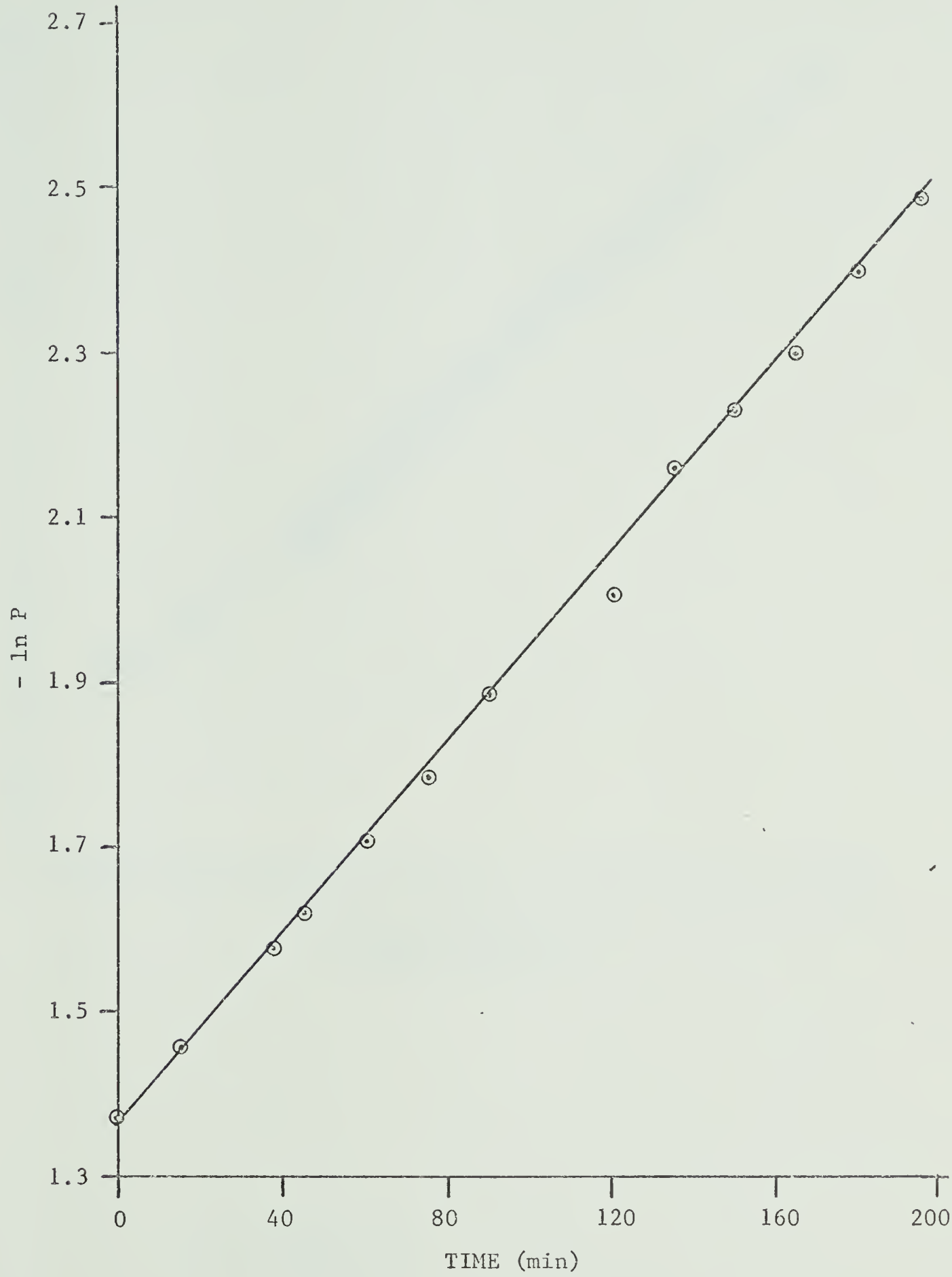
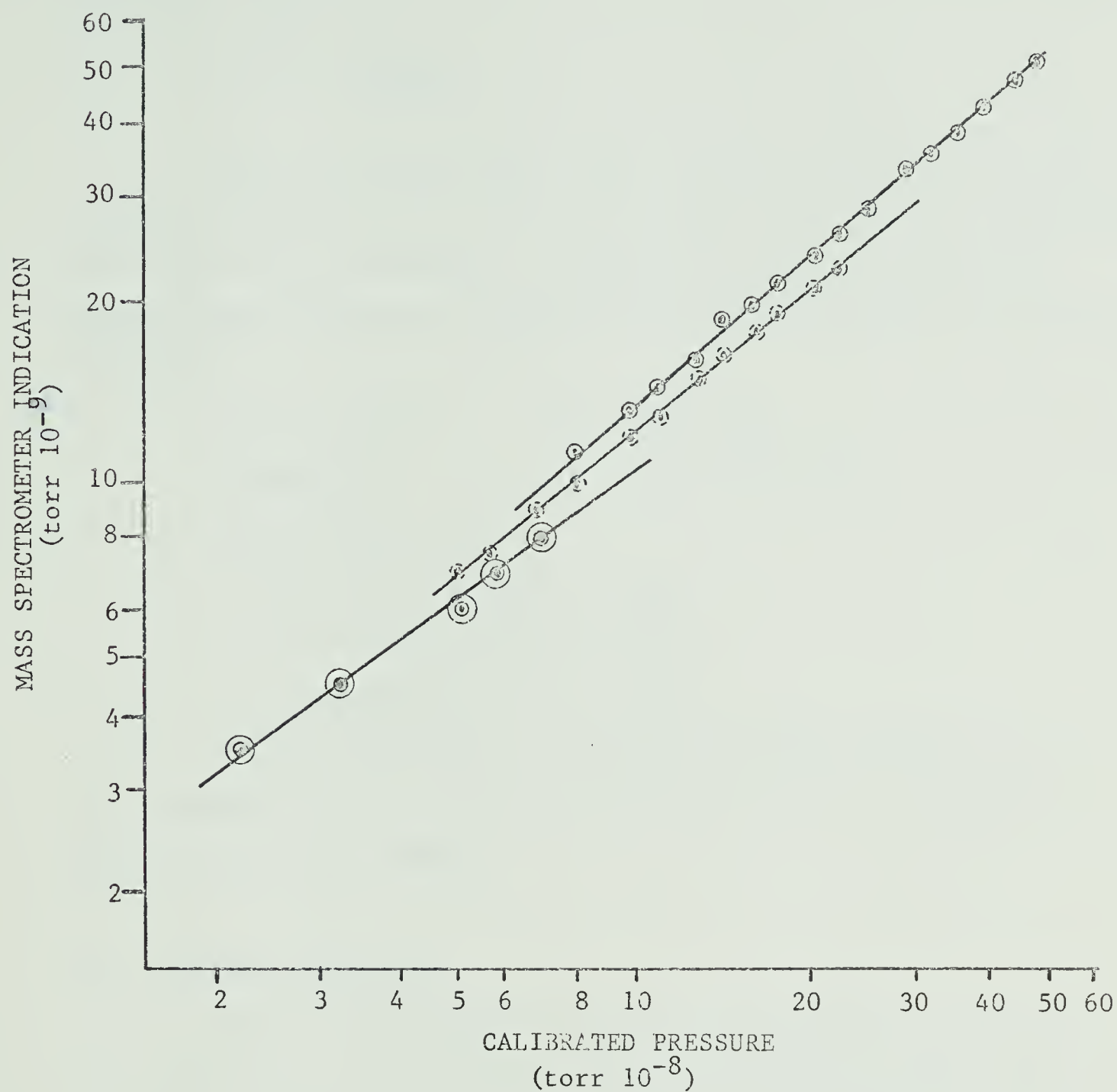


FIGURE 4.5 LEAK VALVE CONDUCTANCE



- - 1 x 10⁻⁷ fsd
- ◉ - 3 x 10⁻⁸ fsd
- ⊗ - 1 x 10⁻⁸ fsd

FIGURE 4.6 CALIBRATION CURVES FOR MASS SPECTROMETER

but again $P_{GHP} \gg P_s$

so
$$P_s = - \frac{C}{S_e} P_{GHP}$$

From the graphs made during a typical calibration of the system, see Figs 4.4, 4.5 and 4.6, it can be seen that the calibration factor does remain constant, an assumption made in deriving the pumping speed equations. The values obtained from Figs 4.4, 4.5 and 4.6 were:

Pumping Speed	$S_e = 3.25 \text{ l/sec}$
Conductance	$C = 6.35 \times 10^{-6} \text{ l/sec}$
Calibration Factor	
$1 \times 10^{-7} \text{ torr fsd}$	$k = 9.61$
$3 \times 10^{-8} \text{ torr fsd}$	$k = 8.75$
$1 \times 10^{-8} \text{ torr fsd}$	$k = 8.34$

This method relies on the accuracy with which the G.H.P. was calibrated, but is the only practical method of calibrating a system in the U.H.V. range.

4.4 Ion Beam Generator

One of the principal components constructed was the ion beam generator. Kit EAI 606, purchased from Nuclide Corporation, contains a selection of stainless steel plates and tubes, alumina rings, spacers and rods which makes possible the construction of a variety of electron and ion beam generators. From this kit the plates chosen for the electrodes were 1.000 inch x 1.000 inch x 0.010 inches. The filament used should be as small as possible to minimize heating effects. It was found that two turns of 0.005 inch thoriated tungsten gave adequate electron emission with only moderate heating of surrounding surfaces. A tungsten mesh, supplied with the kit, was placed as close as possible to the filament to maximize electron

draw-off. A distance of about 0.025 inches was found to give good electron current, but allowed the filament room for stress relief. A 0.625 inch x 1.000 inch tube was initially chosen for the electron anode, but compromising a mono-energetic ion beam for an increased ion current resulted finally in a tube size of 0.625 inches x 0.500 inches long. A tube 0.1875 inches x 0.1875 inches reached into the electron anode, and with a negative potential, extracted ions from the electron anode. Tungsten mesh was welded across the face of this tube to eliminate electrons from the ion focusing stages. The following electrode (plate 6) was intended to accelerate the ions, but is believed to act more as a buffer between the ion extractor and the following stage, (7,8,9), an Einzel lens. The small diameter of the Einzel lens and the last electrode, (10), tend to have a collimating effect on the beam. The last electrode was intended only for collimation, hence the large spacing from the Einzel lens.

The electrodes were connected to a twenty pin feed-through with 0.010 inch stainless steel wire insulated with fibreglass sleeving. Braided copper wire was used for the heavier filament current. The whole assembly was then slid into the port as far as possible.

Rather than performing complex solutions to determine the proper voltage for each electrode, a supply with eight separate variable potentials was made. Potentials for each electrode were adjusted until the desired current and energy spread was obtained. Fig 4.8 shows a set of curves in which the collimator voltage is varied. A current of 1.19×10^{-7} amperes with an energy spread of 1.8 eV for argon was obtained using the 1.000 inch long electron anode.

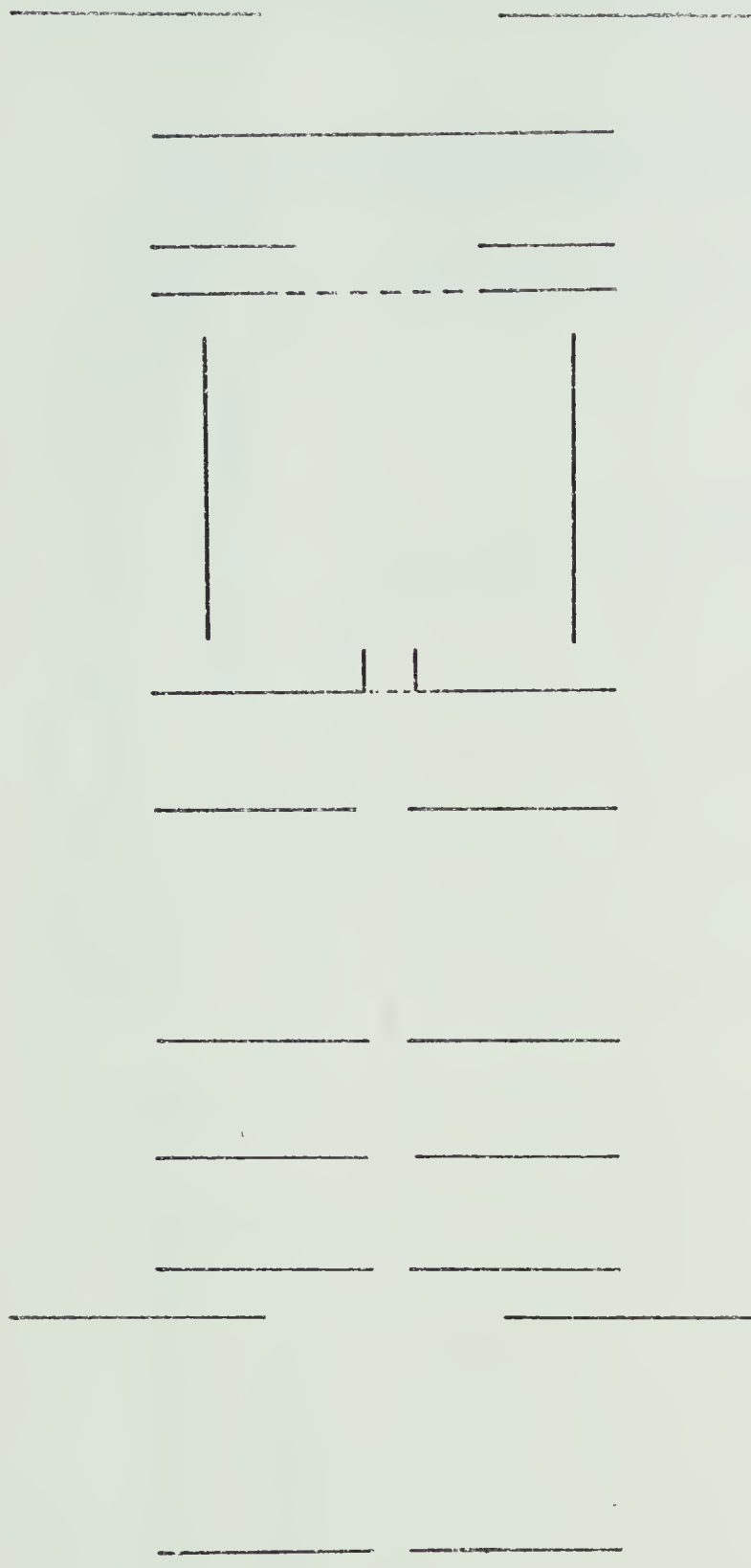
	FUNCTION	<u>ELECTRODE</u> VOLTAGE
	SUPPORT	
	FILAMENT	-37
	ELECTRON ACCELERATOR	+25
	ELECTRON ANODE (ION SOURCE)	0
	ION EXTRACTOR	-0.8
	ACCELERATOR	-10
	EINZEL LENS	-105
	EINZEL LENS	-34
	EINZEL LENS	-105
	SUPPORT	
	COLLIMATOR	-105

FIGURE 4.7 ION BEAM GENERATOR
ELECTRODE CONFIGURATION

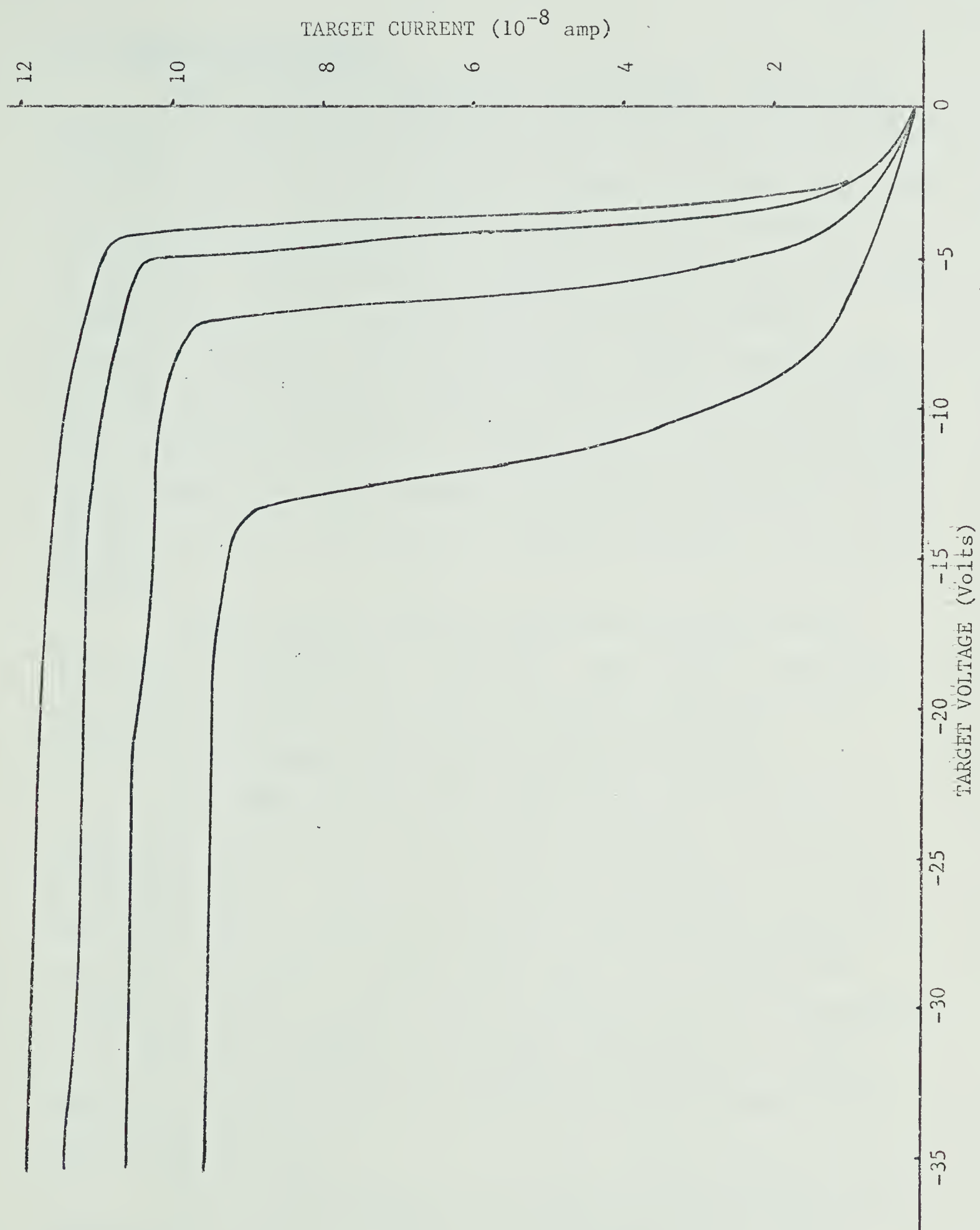


FIGURE 4.8 TYPICAL ION BEAM ENERGY CURVES

4.5 Sample Configurations

Several sample configurations are possible. Intended for mounting on a rotary feed-through which later was found to be defective, a thin-film slide holder was designed and built. The slide tray, made of boron nitride, was machined for a substrate heater and substrate thermocouple. Contacts would be evaporated onto the slide first, then a sample material such as gold would be evaporated between the contacts. Mounted on a rotary feed-through, several different sample materials could be evaluated without opening the system by turning the slide to different evaporators. Possible fields of study include bulk effects such as ion induced changes in resistivity or carrier lifetime studies and surface effects such as trapping efficiency or desorption analyses.

Another type of specimen constructed used metal ribbon 0.001 inches x 0.060 inches x 1.000 inch. Work function variation and annealing studies could be done with this configuration, but, again, it was intended for use with a rotary feed-through.

The sample finally used to demonstrate the facility was a square plate of type 304 stainless steel, 0.6 inches x 0.6 inches x 0.025 inches thick. The plate was mounted perpendicular to the ion beam on a 0.090 inch stainless steel rod. The plate was attached to the rod in essentially a single point weld so as to minimize heat transfer to the rod. A new sample was heated by electron bombardment for several days at 1200⁰ C to thoroughly outgas bulk gas, mainly hydrogen. In addition, it was outgassed for several minutes before each desorption test.

The electron source was ten turns of 0.010 inch thoriated tungsten wire mounted on 0.090 inch stainless steel rods. The filament was placed parallel to the back of the specimen, about 1/8 inch away. An additional stainless steel plate used behind the

filament acted as a reflector to increase the electron current. For a normal desorption test, a current of 10 mA and 1500 volts was used. A current of 30 mA and 1600 volts was used for outgassing.

4.6 Specimen Heating Rate

As shown in chapter three, it is desirable to have a linear temperature increase with time. It was felt that the construction of a temperature function generator was not justified until it was shown that the proposed system was in working order. The temperature curve must be linear only over the temperature interval of interest. Bearing this in mind, it was found that an approximately linear temperature ramp could be generated by electron bombardment heating. Fifteen hundred volts was applied to the specimen, then the filament power was turned on. As a first approximation, it was found that

$$T = 23.5t - 100$$

The error is less than 5% over the temperature range 100° C to 500° C. The temperature curve is more accurately described by

$$T' = 1.179 \times 10^{-3} t'^3 - 0.388 t'^2 + 32.8 t' - 55$$

where $t' = t - 5 \text{ sec}$

$$T' = T - 30^\circ \text{ C}$$

This equation is plotted with the actual temperature in Fig 4.9.

4.7 Detection of Desorbed Gas

An AEI 'Minimass' mass spectrometer selectively monitored desorbed helium for desorption spectra. The mass spectrometer was initially mounted directly on the end port. However, it was found that the mass spectrometer gave a 'reading' as the specimen was heated. This 'reading' was not tuneable and, in fact, it made no difference whether the mass spectrometer filament was on or off. It

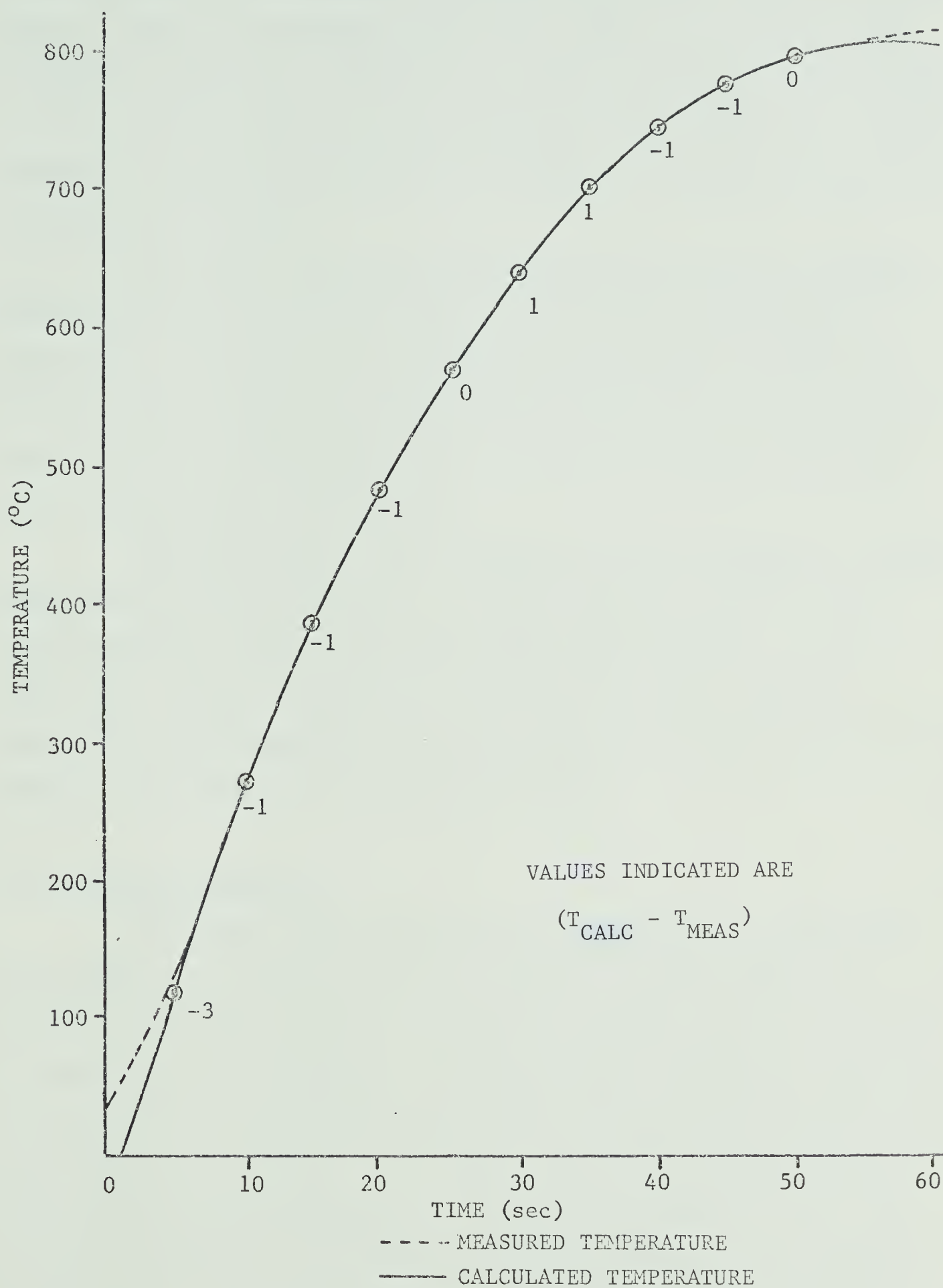


FIGURE 4.9 SPECIMEN TEMPERATURE VERSUS TIME

was found that ion bombardment could produce the same effect to a lesser extent. Further investigation showed the effect to be highly energy dependent, producing an effective ion current at low energies, changing to a net electron current at energies near 1.0 KeV with argon. Simply mounting the mass spectrometer out of sight of the specimen completely eliminated the problem.

The output from the mass spectrometer was fed to a modified MC1439 operational amplifier circuit, see Fig 4.11, operating at a gain of 100. This was fed to a differentiator stage, see Fig 4.12. The high input impedance permitted time constants up to twenty minutes. The output of the differentiator was recorded on a linear time base with a Mosely 7030-A X-Y recorder.

The differentiator was calibrated using a triangular waveform from an Exact Function Generator. Differentiator input and output were recorded on a Mosely 7010 dual trace strip recorder. It was found that 1 mV/sec input produced 3.58 volts output. The mass spectrometer produced 98.6 mV at full scale deflection, hence differentiator readings can be converted to desorption rates.

4.8 Operating Procedure

The normal operating procedure for a desorption experiment was as follows. Following thorough outgassing of the sample, the titanium sublimation pump was cycled if the chamber was to be isolated for more than several minutes. Helium was then admitted to volume V_3 of the G.H.P. to a pressure of about 500 microns, and the liquid nitrogen cold trap, CT2, was filled. The chamber was then isolated with the main valve and helium admitted to an indicated pressure of 10^{-5} torr via the leak valve. The desired bombarding voltage was then applied to the sample. The elapsed timer was started when high voltage was applied to the ion beam generator. Following the desired bombardment,

the chamber was evacuated to a pressure of less than 4×10^{-10} torr, with the mass spectrometer now turned on. The chamber was again isolated, +1500 volts applied the sample (+1500 volts when under a 10 mA load) and the X-Y recorder started. At a given point in the recorder sweep, the filament power was applied. Following the desorption sweep, the chamber was again evacuated. It was found that applying 30 mA at 1600 volts for several minutes was adequate to clean the specimen of helium for the low bombarding energies used. Cooling curves showed that the sample approached room temperature within one half hour of outgassing.

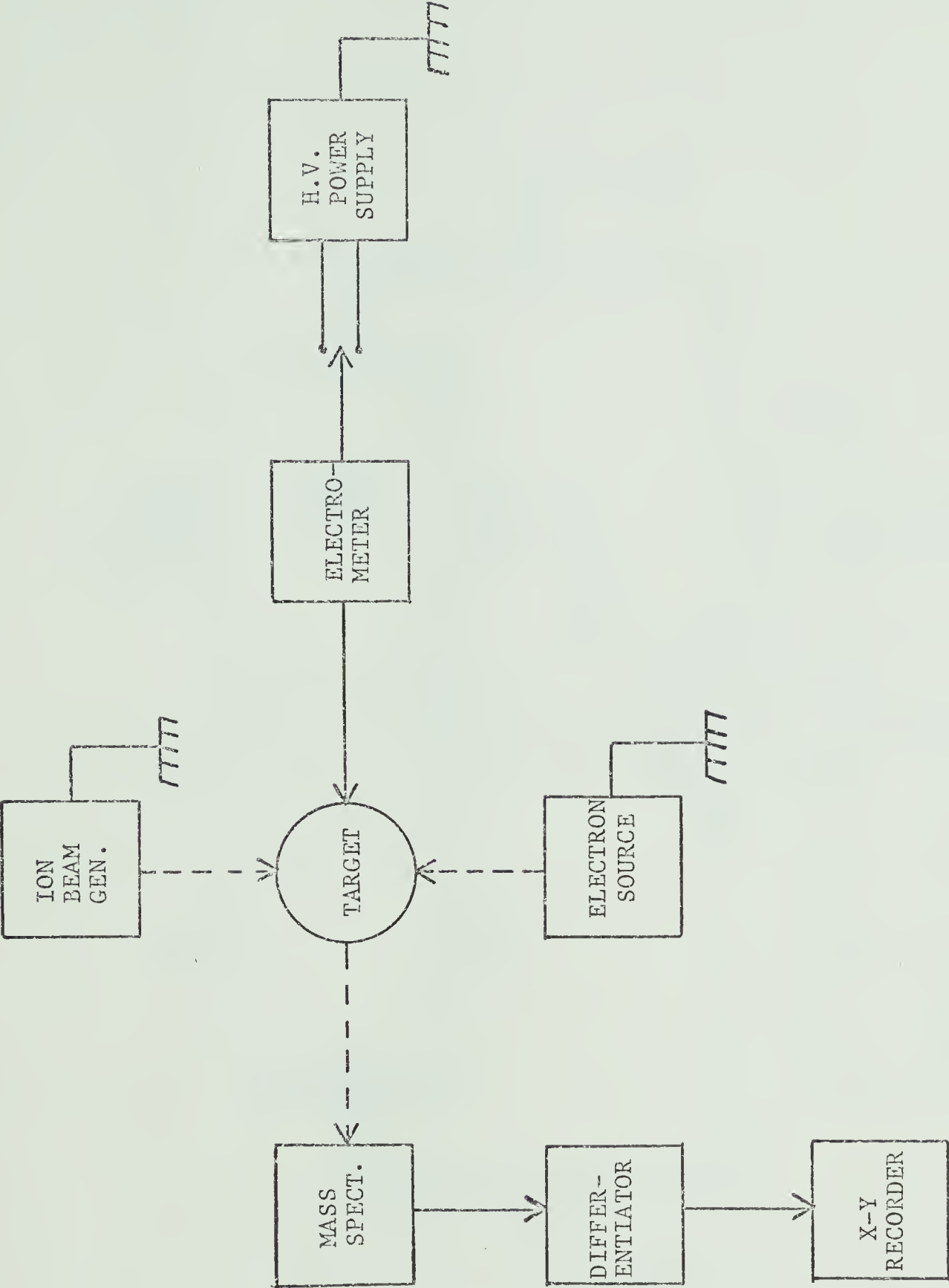


FIGURE 4.10 OPERATIONAL BLOCK DIAGRAM

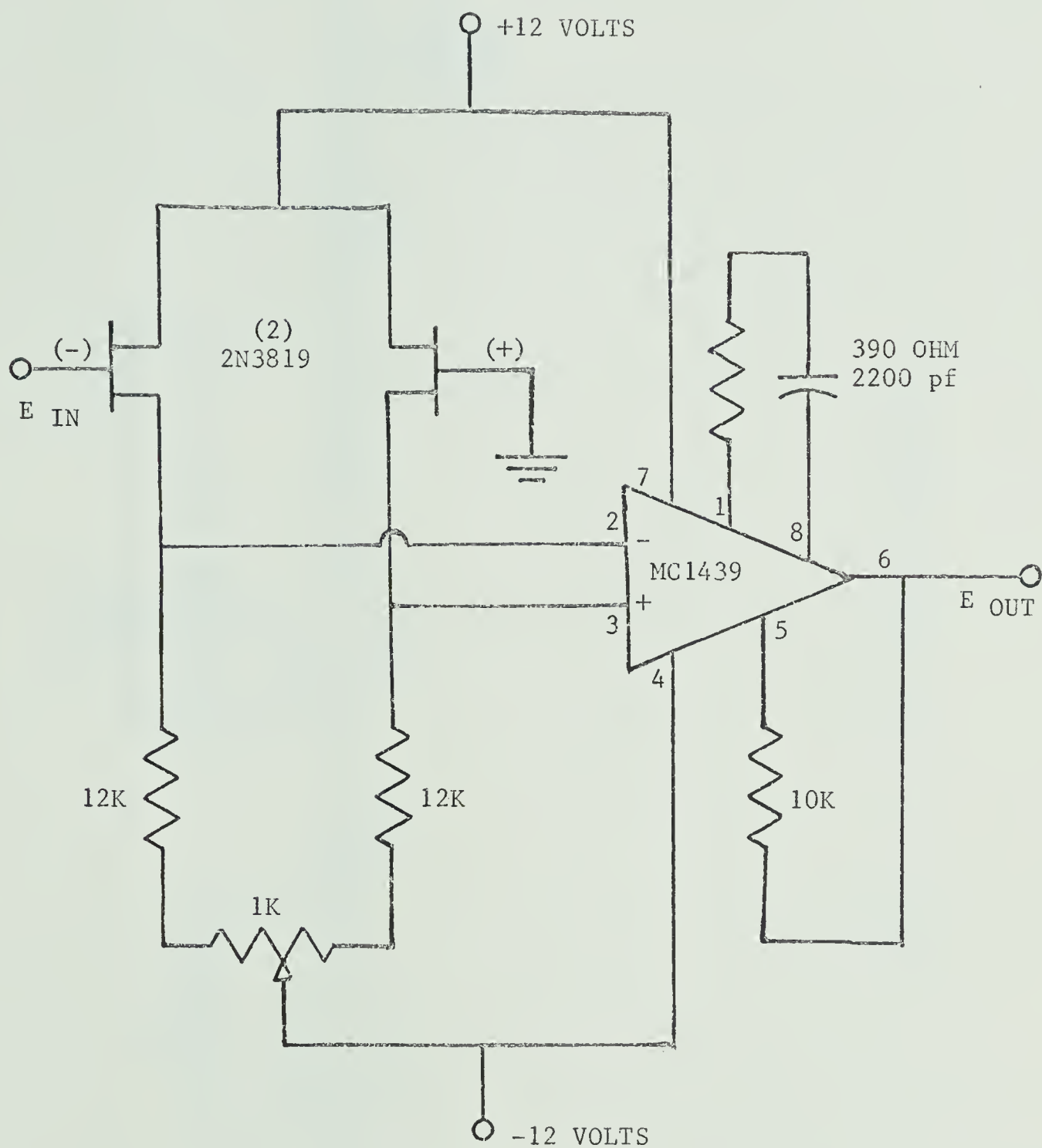


FIGURE 4.11 HIGH IMPEDANCE OPERATIONAL AMPLIFIER

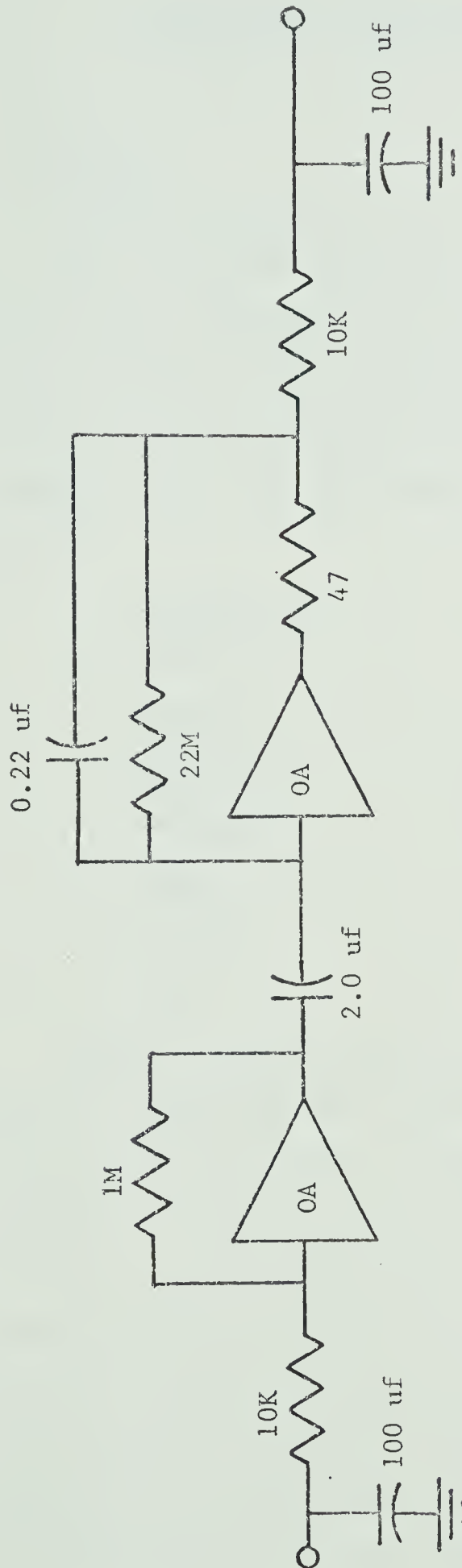


FIGURE 4.12 DIFFERENTIATOR SCHEMATIC

CHAPTER 5

EXPERIMENTAL RESULTS AND DISCUSSION5.1 Introduction

Although stainless steel is widely used for UHV systems and for laser and plasma electrodes, little study has been done on stainless steel, other than on its basic physical properties.

Stainless steel has a fcc structure at room temperature, is nearly non-magnetic and has a melting point of 1400°C to 1450°C . Type 304, commonly used in vacuum systems, has the following nominal composition:

Chromium	18 - 20% max
Nickel	8 - 12%
Carbon	0.08% max
Manganese	2.0% max
Phosphorus	0.045% max
Sulphur	0.03% max
Silicon	1.0% max, and
Iron	68%

Helium, commonly used in laser and plasma research, was chosen as the bombarding gas because it gives better resolution for desorption spectra and shows no sign of saturation at doses up to 10^{16} ions/cm² in tungsten. The relatively large area of the target could result in a non-uniform dose across the plate, but ion doses used were generally two orders of magnitude less than 10^{16} ions/cm², so saturation should not be a problem. Lucasson and Walker²¹ found that the threshold displacement energy for bcc iron is 24 eV. Thus, an incident energy greater than 96 eV is necessary to displace a lattice atom. By bombarding with ions having less than this energy, it is

possible to place helium in the target without substantially damaging the target and study defects intrinsic to the target. A comparison of damaged and undamaged trapping sites can be made by comparing, for instance, a 75 eV curve with a 500 eV curve.

5.2 Experimental Results

The desorption spectra obtained with helium in this work are shown in Fig 5.4 through to 5.10. Comparing these with the desorption spectra using argon, Fig 5.3, the difference in resolution is quite clear. The dose referred to in the diagrams is calculated from measured target current. Secondary emission reduces this to a value

$$\begin{aligned} n(\text{true}) &= \frac{n(\text{meas})}{(1+\epsilon)} \\ &= 0.8n(\text{meas}) \end{aligned}$$

The same dose and annealing schedule was used for argon, Fig 5.3, and helium, Figs 5.6, 5.7 and 5.8, but whereas helium spectra clearly show four peaks, only one peak and slight effects from a second peak are found in the argon spectra. Referring to the helium desorption spectra, it can be seen that at low doses and low energy, only two peaks are produced. At successively higher energies and dose, two more peaks begin to form, then become larger in amplitude than the first two peaks and finally account for almost all of the gas desorbed. For ease of identification, these peaks have been labelled α_1 , α_2 , η and β for successively larger activation energies.

It should be noted that α_1 and α_2 appear in the 75 eV spectra. The maximum energy transfer to iron at this incident energy is 18.7 eV. Since the incident ions will be unable to displace iron atoms from their lattice site, then α_1 and α_2 are indicative of trapping sites in an undamaged target.

FIGURE 5.1

Results from Argon Desorption	
Incident Energy	Activation Energy
200 eV	1.65 eV
300 eV	1.82 eV
400 eV	1.87 eV
500 eV	1.98 eV

FIGURE 5.2

Results from Helium Desorption	
Peak	Energy
α_1	1.16 eV
α_2	2.00 eV
γ	2.68 eV
β	2.98 to 3.08 eV

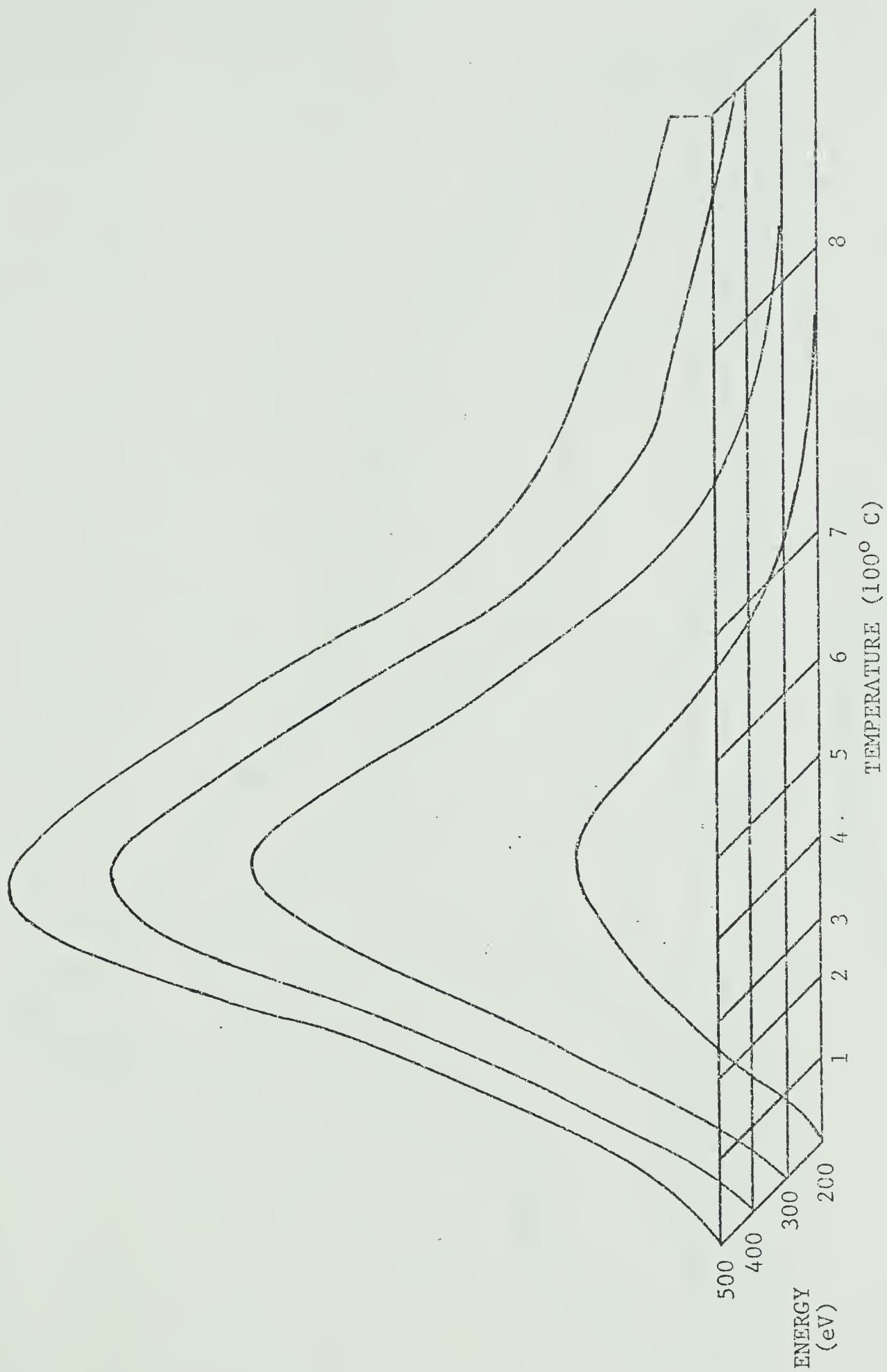


FIGURE 5.3 ARGON DESORPTION
CONSTANT DOSE 2×10^{14} IONS/cm²

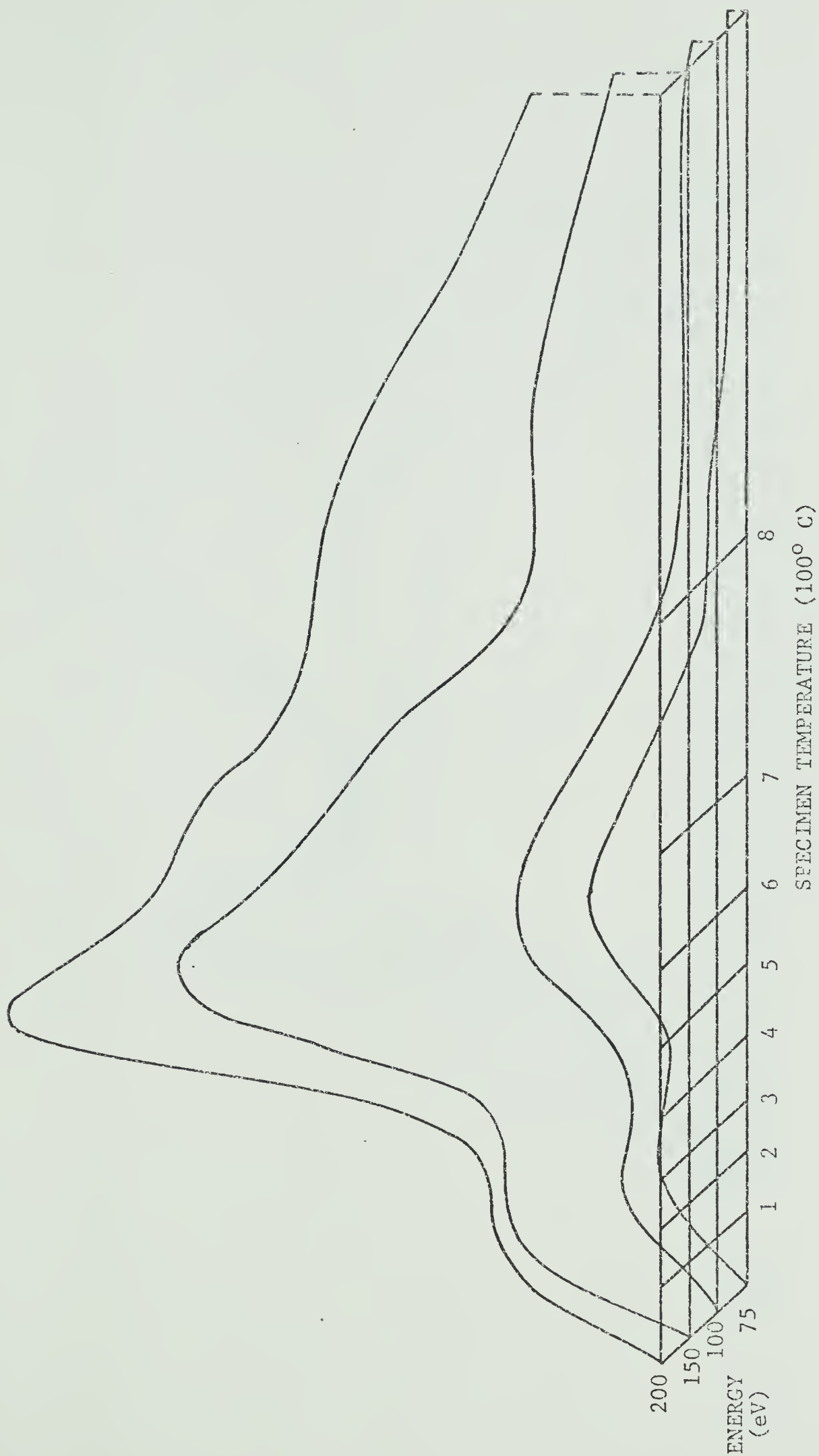


FIGURE 5.4 HELIUM DESORPTION
CONSTANT DOSE 1×10^{14} IONS/ cm^2

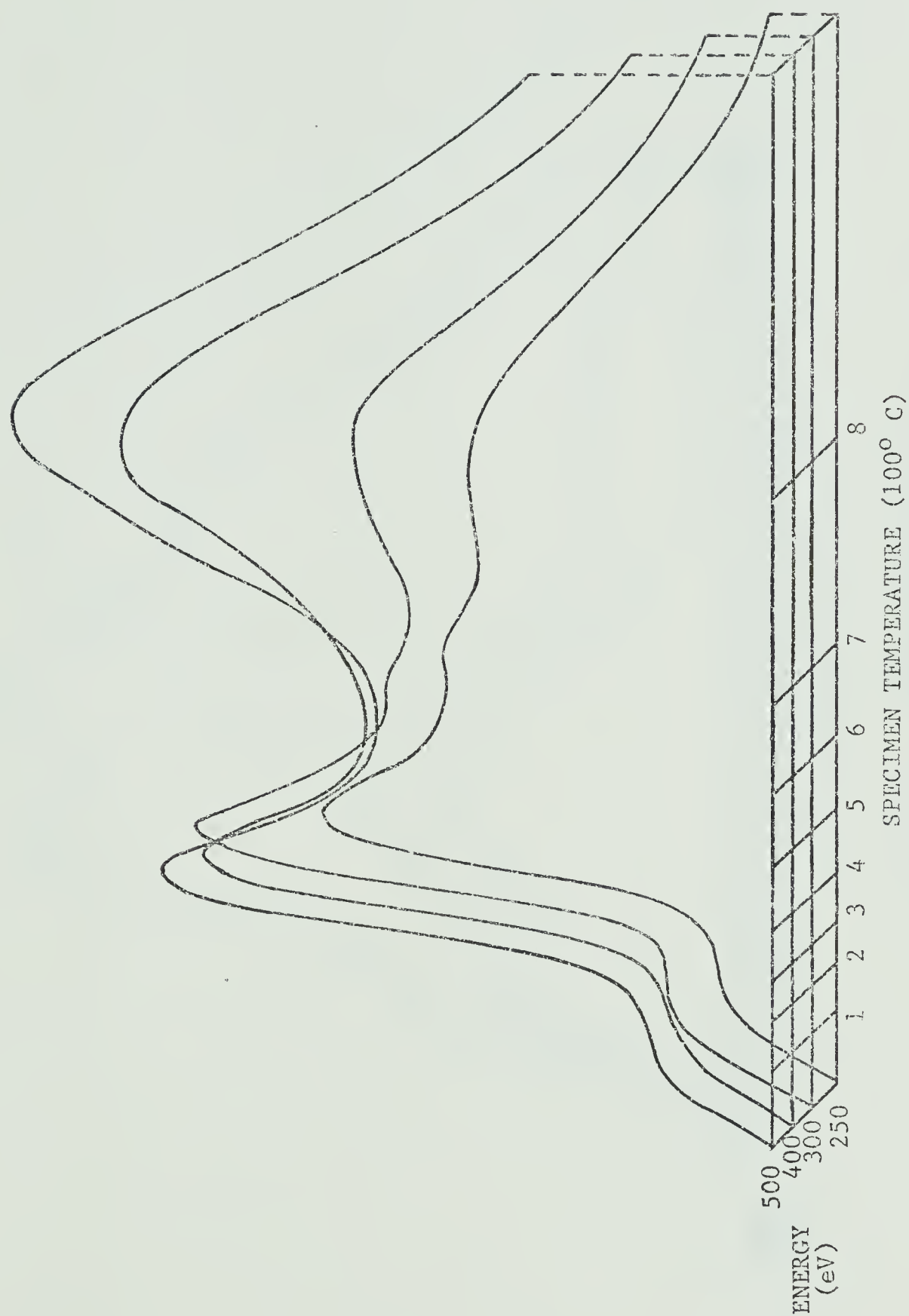


FIGURE 5.5 HELIUM DESORPTION
CONSTANT DOSE 1×10^{14} IONS/ cm^2

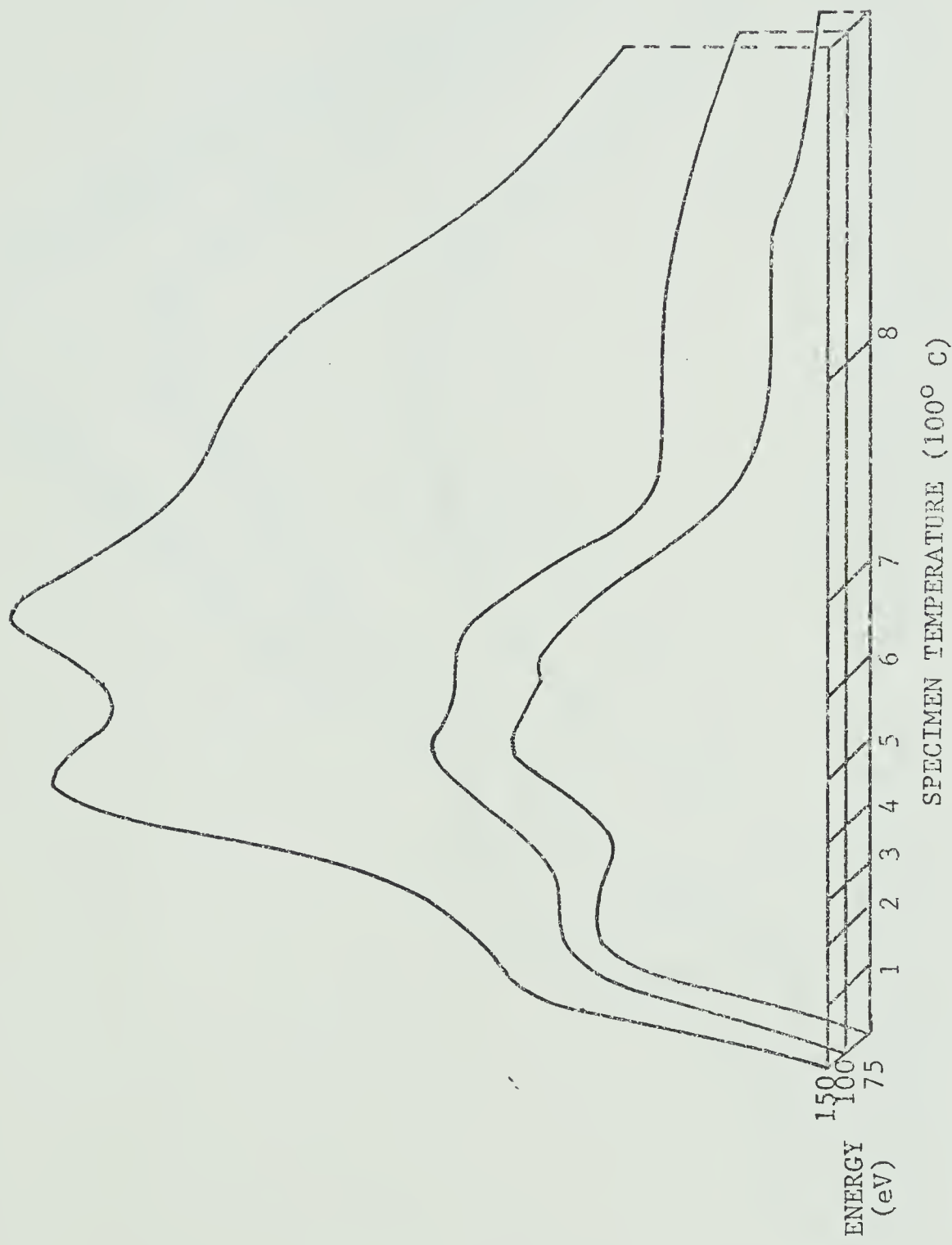


FIGURE 5.6 HELIUM DESORPTION
CONSTANT DOSE 2×10^{14} IONS/cm²

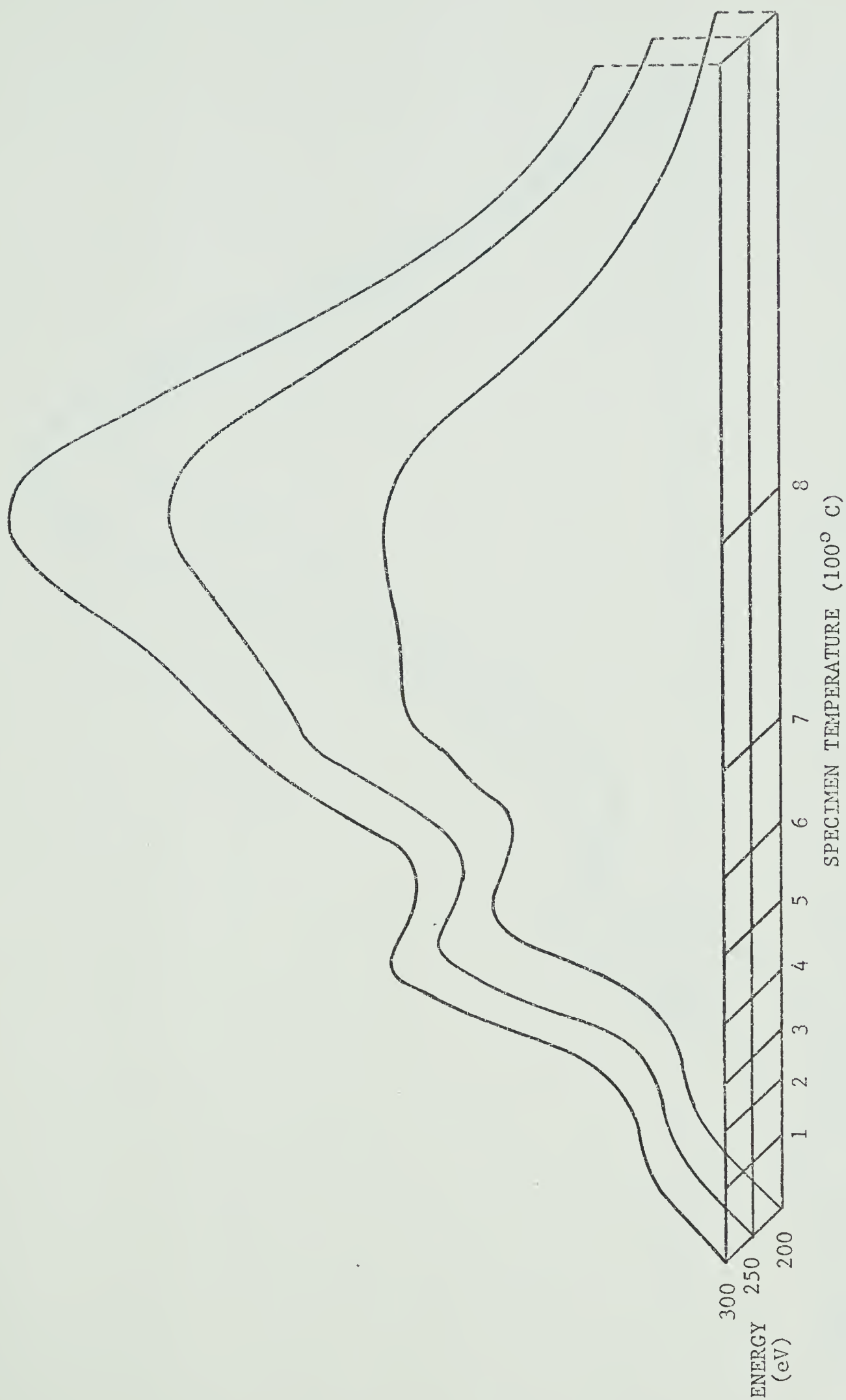


FIGURE 5.7 HELIUM DESORPTION
CONSTANT DOSE 2×10^{14} IONS/ cm^2

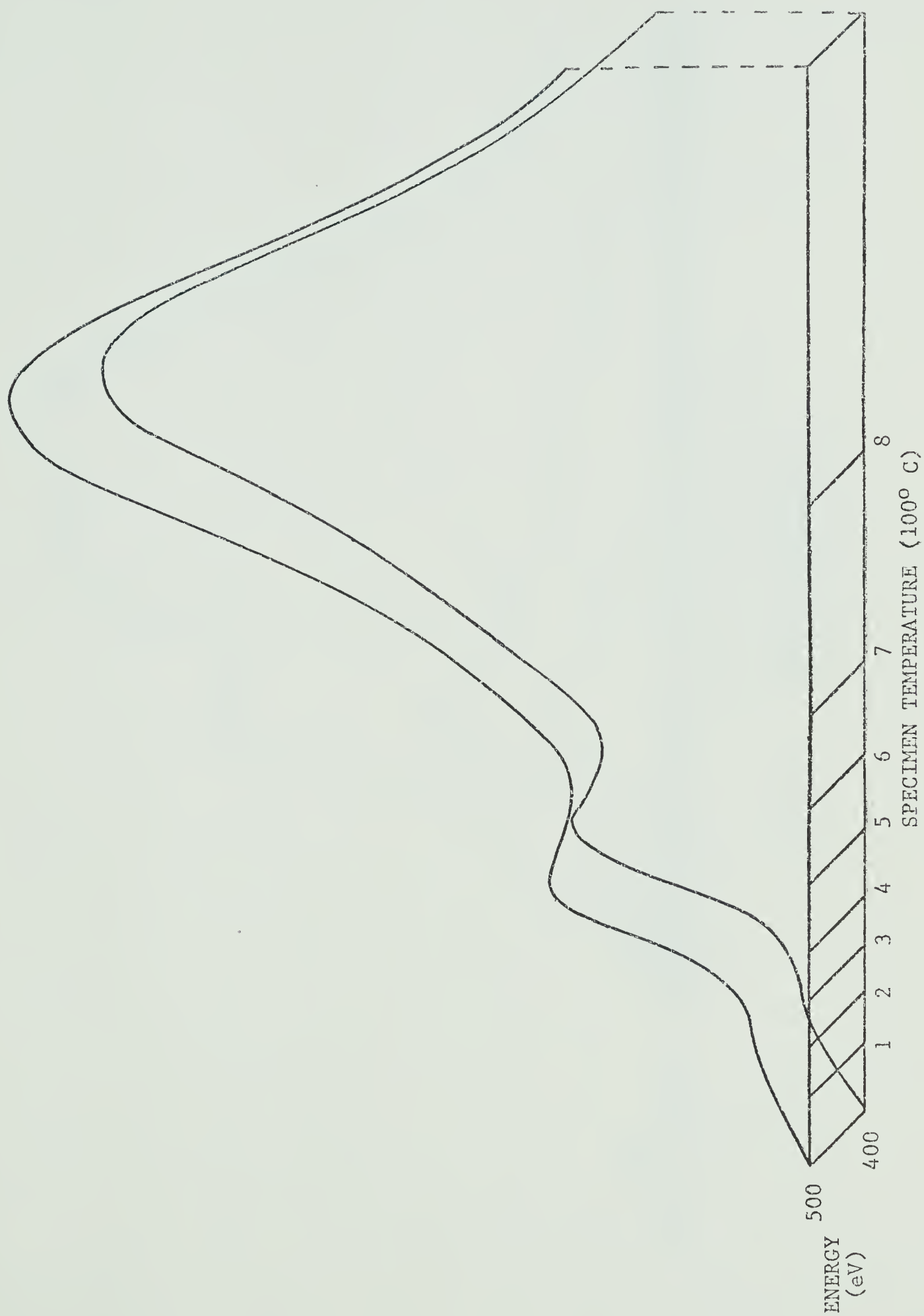


FIGURE 5.8 HELIUM DESORPTION
CONSTANT DOSE 2×10^{14} IONS/cm²

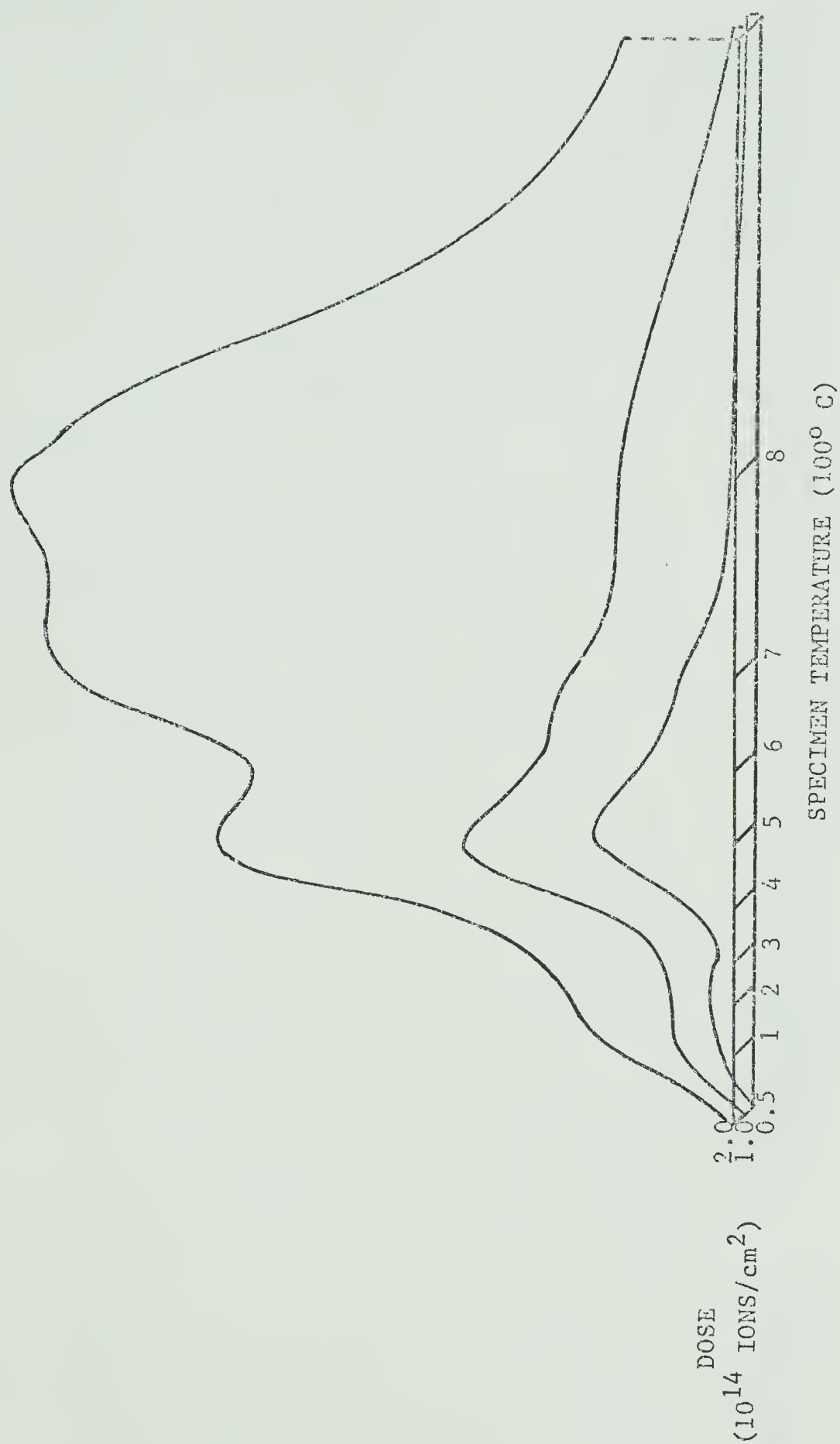


FIGURE 5.9 HELIUM DESORPTION
CONSTANT ENERGY 200 eV

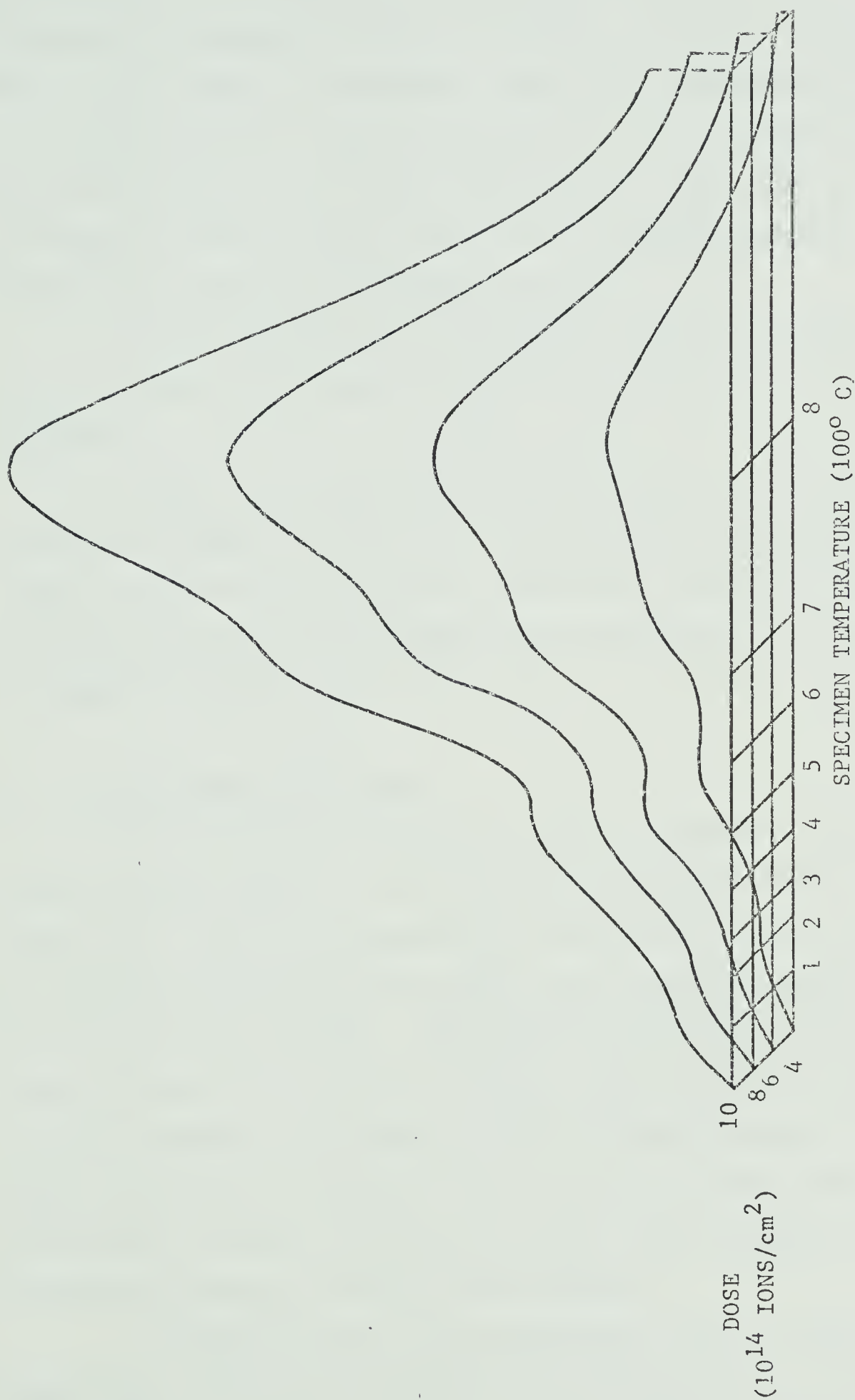


FIGURE 5.10 HELIUM DESORPTION
CONSTANT ENERGY 200 eV

For a constant dose of 1.0×10^{14} ions/cm², α_2 dominates up to 300 eV. It appears to saturate and actually decreases in amplitude for energies greater than 300 eV. It must be emphasized that α_2 only appears to saturate. This will be explained later. The η peak has only a minor contribution to gas desorption at this dose and is found in the 200, 250 and 300 eV curves. The β peak is found at energies greater than 200 eV and becomes the greatest source of gas in the 400 and 500 eV curves.

Similar spectra are produced for a dose of 2×10^{14} ions/cm² but the η peak is more pronounced at this higher dose, see Fig 5.7 and 5.8.

Figs 5.9 and 5.10 show the dependence of the spectra on dose over a range 5×10^{13} to 1×10^{15} ions/cm². An incident ion energy of 200 eV was used for all curves but η and β become the principal gas source at high doses just as they did in the case of the higher energy spectra.

5.3 Interpretation of Results

In analysing the results, visual examination reveals several characteristics of the desorption reactions. The activation energy for α_1 and α_2 is independent of dose and incident energy. The increase in desorption rate, $\frac{dn}{dt}$, for α_1 and α_2 is slower than that for the η and β peaks. These observations indicate that α_1 and α_2 are due to first order reactions. The η reaction is harder to determine because of the masking effect of the β reaction, so more detailed analysis is necessary. The β reaction shows a steady increase in activation energy with higher dose and a rapid increase in η with dose which indicates a second order reaction.

In chapter three it was stated that a plot of $\log (n_0 T_p^2)$ against $\frac{1}{T_p}$ results in a straight line if the reaction is second order and the slope of the line will be $S = \frac{E}{R}$. This was intended for

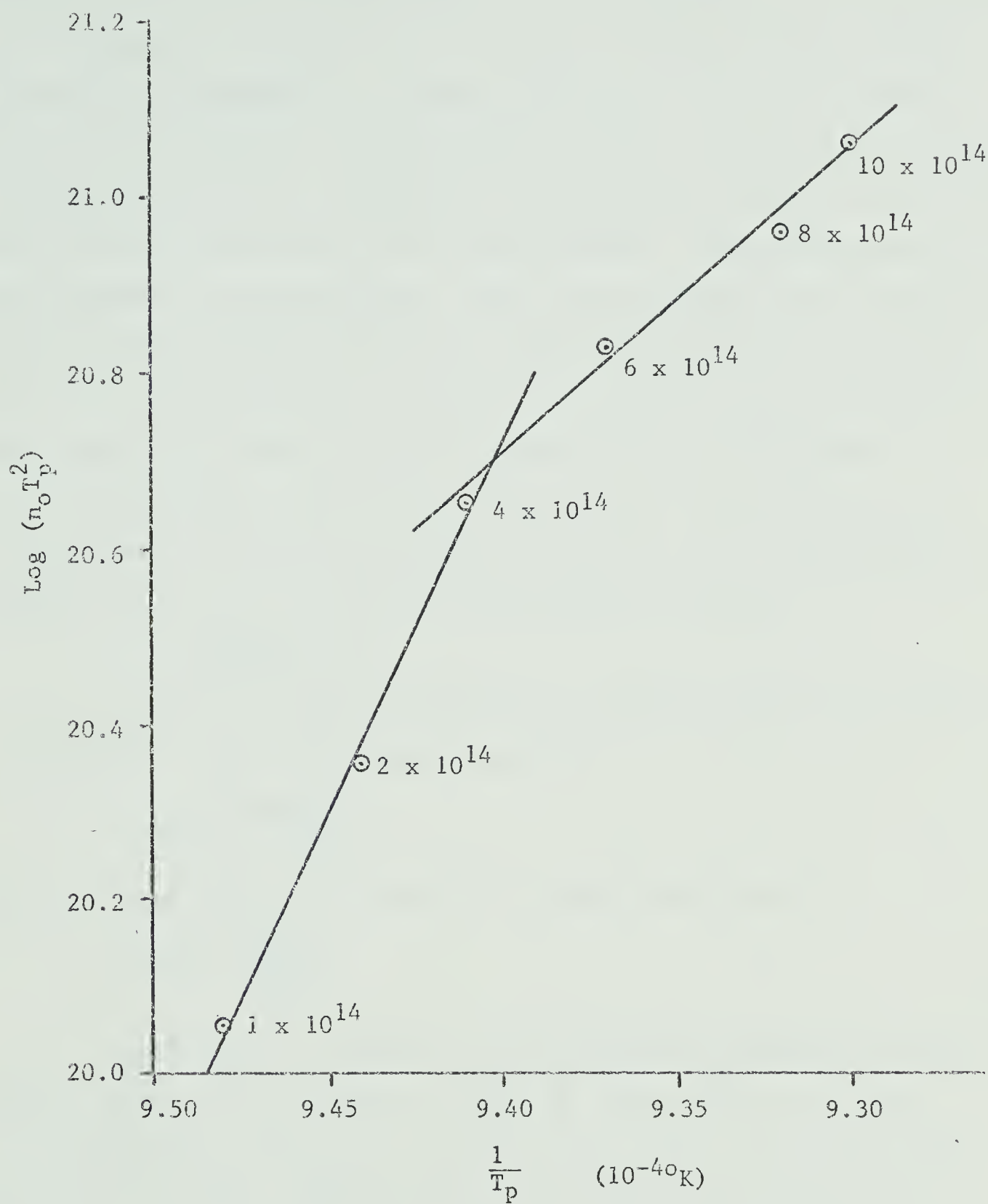


FIGURE 5.11 $\text{LOG } (n_o T_p^2)$ VERSUS $\frac{1}{T_p}$

isolated peaks and the application of this procedure to the β reaction is distorted by a division of the increase in dose amongst several trapping configurations. As shown in Fig 5.11, two nearly linear sections are produced. The first points yield an apparent activation energy of 7.45 eV, but referring to the desorption spectra, one finds that α_2 is trapping most of the dose increase. The temperature shift is a function of dose increase. Thus, the temperature shift measured will be smaller than expected for a given dose increase because only part of the dose increase is trapped in β sites. It is easily shown that this will be plotted as a reaction with higher-than-real activation energy. When the β peak dominates, a straight line is obtained with an activation energy of 3.02 eV. This agrees with the values 2.98 to 3.04 eV obtained from Redhead's relation

$$E = \left(\frac{0.065}{23}\right) T_{\max}$$

Another method of checking the reaction order is indicated by Carter ¹⁰. For a first order reaction

$$\dot{n}_{\max} \approx \frac{n_{i0} b E_i}{RT_p^2}$$

which is linear in n_{i0} , whereas for a second order reaction

$$\dot{n}_{\max} \approx \frac{b E n_{i0}}{4RT_p^2}$$

However, T_p is known to be a function of initial dose n_{i0} . Thus, a plot of \dot{n}_{\max} against n_{i0} will be linear only for a first order reaction. As expected, α_1 and α_2 are found to be linear and β is concave upwards, indicating that the order of the reaction is greater than one. The η peak is also concave upwards, although not to such a high degree, but the part of the curve corresponding to doses 6×10^{14} to 1×10^{15} ions/cm² is linear.

Using $\dot{n} = n^x v_x e^{-E/RT}$, a log - log plot of \dot{n} versus dose will have a slope

$$\frac{\ln \dot{n}}{\ln n} = x + \frac{\ln v - E/RT}{\ln n}$$

But $\ln v \gg E/RT$

$$\text{So } \frac{\ln v - E/RT}{\ln n} \approx \frac{\log v}{\log n}$$

For a dose variation of 5×10^{13} to 1×10^{15}

$\frac{\log v}{\log n}$ takes values from 1.05 to 1.15

Thus, $\frac{\Delta \ln \dot{n}}{\Delta \ln n} \approx x$, the order of the reaction.

The slopes of the plots in Fig 5.13 are

$$S\alpha_1 = 0.96,$$

$$S\alpha_2 = 0.835,$$

$$S\eta = 1.145,$$

$$\text{and } S\beta = 1.509.$$

These results indicate that α_1 and α_2 and η are first order peaks while β is a function of $n^{3/2}$. This could result from two independent additive reactions, one first order and the other second order. A reaction with E dependent on dose will not yield a linear plot, but Fig 5.13 shows all plots to be linear, within experimental limits.

At higher doses, there is a greater probability of striking a previously trapped helium atom. From the relation

$$E_T = \frac{4m_1m_2}{(m_1+m_2)^2} E$$

one can see that it is possible to transfer all incident energy to a trapped helium atom. Thus, an incident helium ion is able to displace and knock other helium atoms to greater depths when it does not possess sufficient energy to displace an iron atom. For a constant incident energy, the depth distribution should not change if ions remain where they were first trapped, but the curves of increasing dose with constant energy clearly show that β shifts to higher activation energy with increasing dose. Since diffusion is a second order reaction, this, and previously explained results, indicate that β is due to bulk diffusion of helium in stainless steel. Diffusion is believed to originate from sites farther than three lattice spacings

from the surface. Helium, because of its small radius and mass, will have deep penetration for a given incident energy. At higher energies, an incident ion has a high probability of travelling beyond the para-surface. Kornelson has found that penetration varies as $E^{3/2}$ along channel directions. Ions trapped more deeply will require a higher energy for diffusive release ⁷. This corresponds to the temperature shift that β exhibits for progressively higher incident energies. Birchenall and Mehl ²² found the self-diffusion energy of γ -iron to be 2.09 eV in a temperature range of 935 - 1112° C, and a self-diffusion energy of 3.35 eV in the temperature range 785 - 887° C for α -iron. Later, Borg and Birchenall ²³ found the diffusion energy of α -iron to be 2.92 eV in the temperature range 785 - 880° C. Although α_2 has an energy near that for self-diffusion in γ -iron, temperatures used for desorption tests were below 840° C. In addition, α_2 is a first order reaction, whereas diffusion is second order. The activation energy and temperature range for self-diffusion in α -iron does correspond to β . It now appears that the target behaves more like α -iron than γ -iron.

Despite the composition of stainless steel stated earlier in this chapter, it is very difficult to predict the composition of the steel after many annealing cycles, however, due to phase relationships of steel alloys. Phase diagrams ⁸ show that carbon should precipitate at temperatures less than 835° C for an 18 - 8 type stainless steel with 0.08% carbon. In normal production, the steel is quenched quickly and the carbon remains in solution. If cooled slowly or held at 650° C for a short time, carbon precipitates as chromium carbide, usually at grain boundaries. Lacking sufficient chromium and nickel, normal austenitic steel becomes unstable at temperatures lower than 723° C and changes to a body centered structure but the carbon remains in solution. Hence a body centered tetragonal structure is formed.

The bcc steel (martensite) is metastable, and must be quench formed to avoid formation of ferrite (bcc) and carbide.

From the above discussion, it is to be expected that a chromium carbide precipitate shall form at grain boundaries because of the large cooling time-constant of the target in the vacuum system. Chromium is not as mobile in steel as carbon and regions adjacent to grain boundaries will be depleted of chromium. It is possible that the resulting chromium-nickel imbalance will result in the formation of a body centered structure.

A specimen that underwent many annealing cycles and later was taken from the system was found to have similar magnetic properties to original target material. This indicates that an annealed target essentially retains its stainless steel non-magnetic properties despite indications of a phase change on a large portion of the surface.

The characteristics of η are indicative of ion-induced surface damage. Its presence only in the range 100 eV to 300 eV would suggest that a threshold energy must be exceeded before damage can be done. At a dose of 2×10^{14} , η begins to desorb gas with an incident energy of 100 eV. This agrees with the value of 24 eV obtained by Lucasson and Walker ²¹ for a displacement threshold energy in bcc iron. The collision cross-section of an incident ion decreases rapidly at energies below 1 KeV⁷. Thus, from Figs 5.7 and 5.8, it appears that for energies greater than 400 eV, helium has few collisions with surface atoms and easily penetrates beyond the surface. Another feature of η is its dose dependence. Comparing the 1×10^{14} and 2×10^{14} curves, one finds the η peak more dominant in the higher dose, but it is overridden by β in the 400 and 500 eV curves. Looking at variations in dose, however, one finds that η is visible in all but the 5×10^{13} curve. It is believed that bombardment induced surface damage promotes para-surface bubble formation at high concentrations. Truhlar et al ²⁴ say bubble diffusion should occur in nickel near 2.67 eV, but no peak was found using argon and krypton in their work.

This energy agrees with the value 2.68 eV found using helium.

Bubble formation is more likely with helium because of its high mobility and, thus, its greater ability to aggregate.

A reduction in collision cross-section with energy is also evident for α_1 and α_2 in Figs 5.6, 5.7 and 5.8. The maximum desorption rate increases with incident ion energy to 250 eV or 300 eV. For higher energies, α_1 and α_2 begin to decrease in amplitude. As stated earlier, α_1 and α_2 appear to saturate, but if α_1 and α_2 are due to surface trapped helium their decrease is more readily explained by a decrease in incident ion collision-cross-section, which results in fewer collisions with surface atoms. If a lattice defect is involved in a reaction with a trapping site, the lattice defect must interact with the particular trapped atom that produced it in a first order reaction. This implies that α_1 and α_2 trapping sites are very close to the surface. Kornelson¹³ believes desorption from such sites is by a single activated step. Gas release from surface trapping sites can be due to interstitial or vacancy migration, and dislocation loops. The activation energy 1.16 eV for α_1 agrees with values for interstitial migration or atomic migration along terraces²⁵ in other metals. Vacancy migration is most likely the cause of α_2 . The results obtained show more gas is released by vacancy migration than by interstitial migration in both the damaged and undamaged state. It is known that the surface is a vacancy rich source²⁶. Helium has a high backscattering angle because of its low mass. Thus, even at high energies when few collisions occur at the surface, helium ions may be backscattered and captured in vacancies just below the surface.

Insufficient data was obtained with argon to fully assess Fig 5.3, its purpose being to illustrate the difference in resolution between helium and argon at low energies.

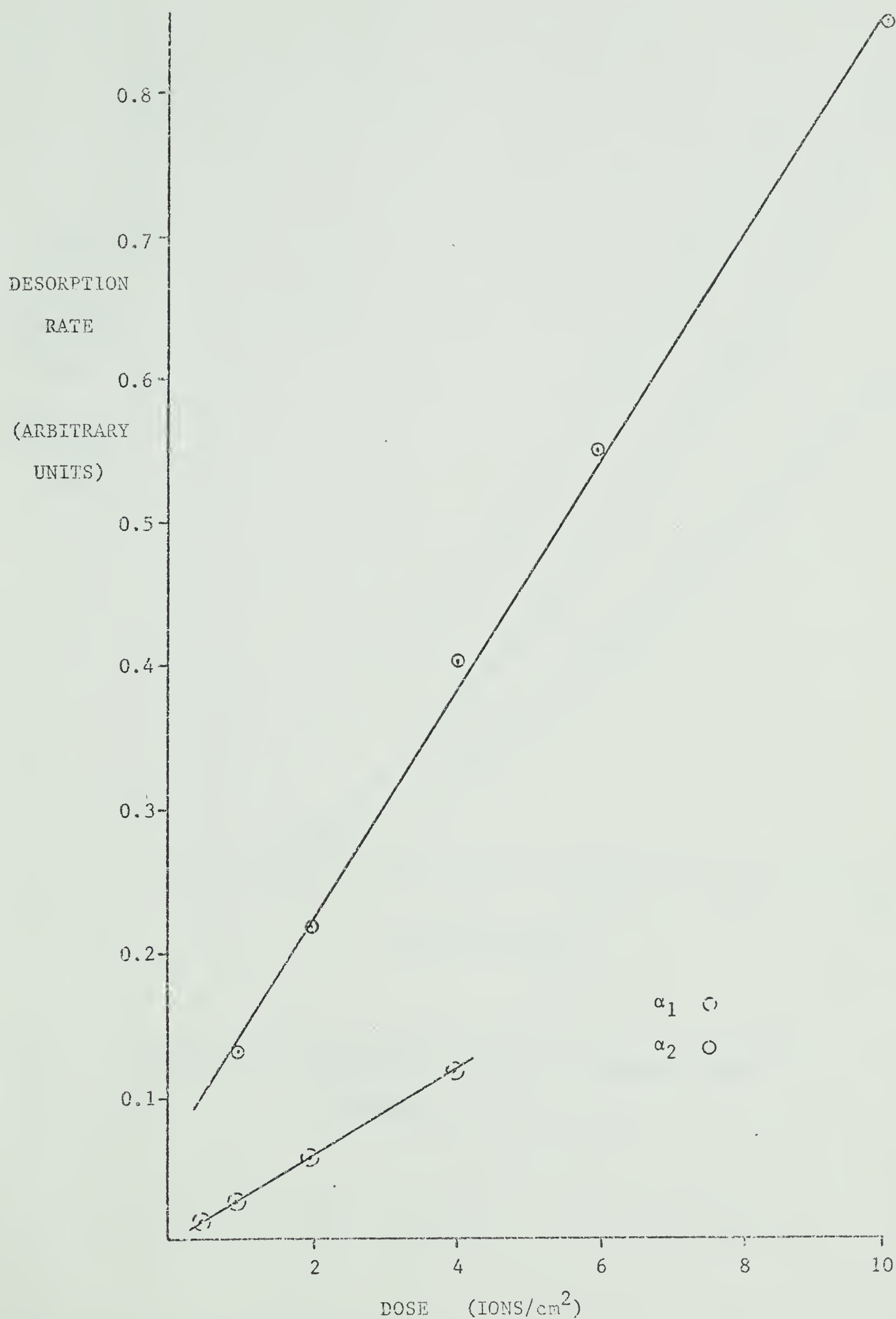


FIGURE 5.12a DESORPTION RATE AS A FUNCTION OF DOSE (LINEAR)

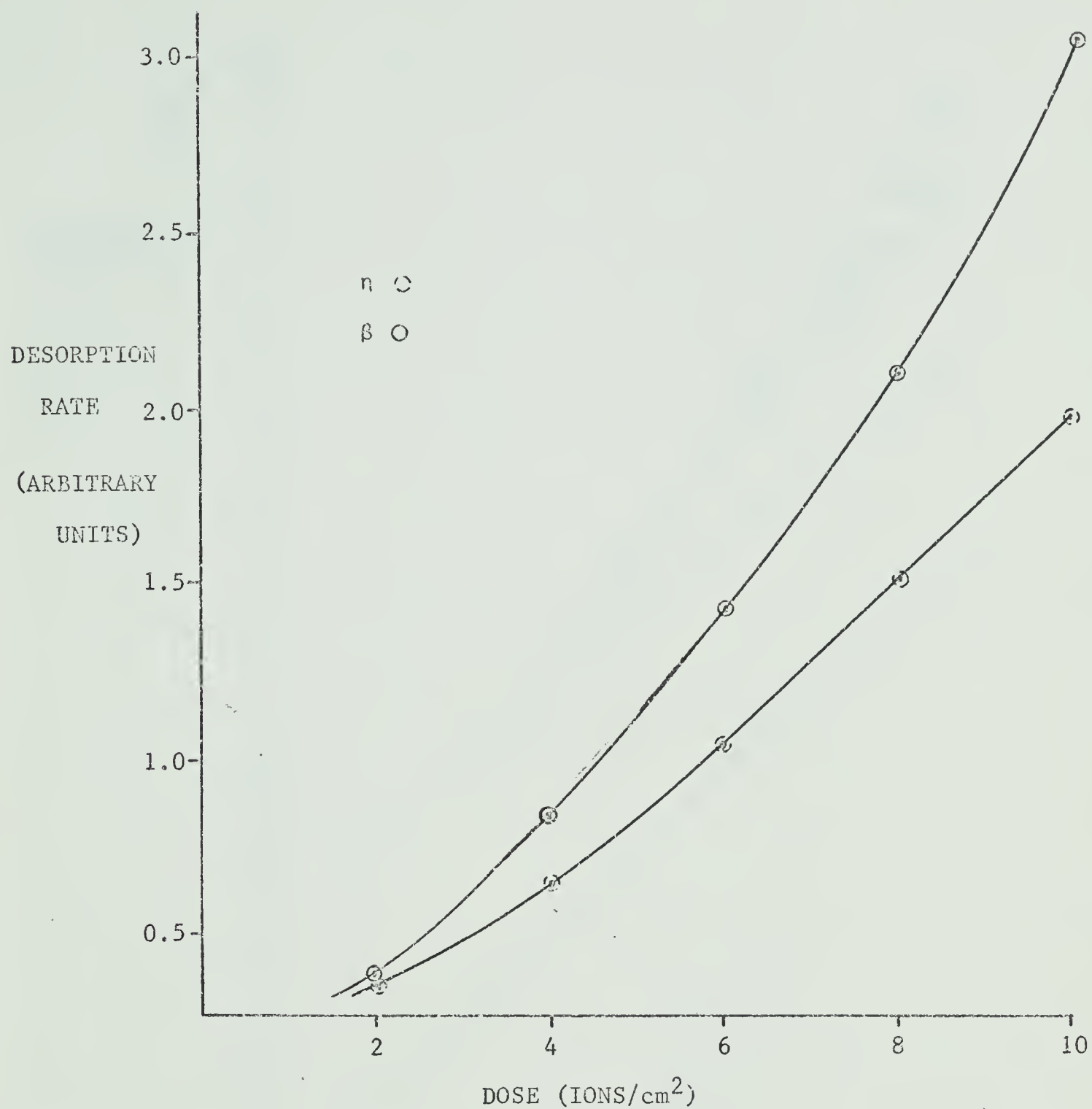


FIGURE 5.12b DESORPTION RATE AS A FUNCTION OF DOSE
(LINEAR)

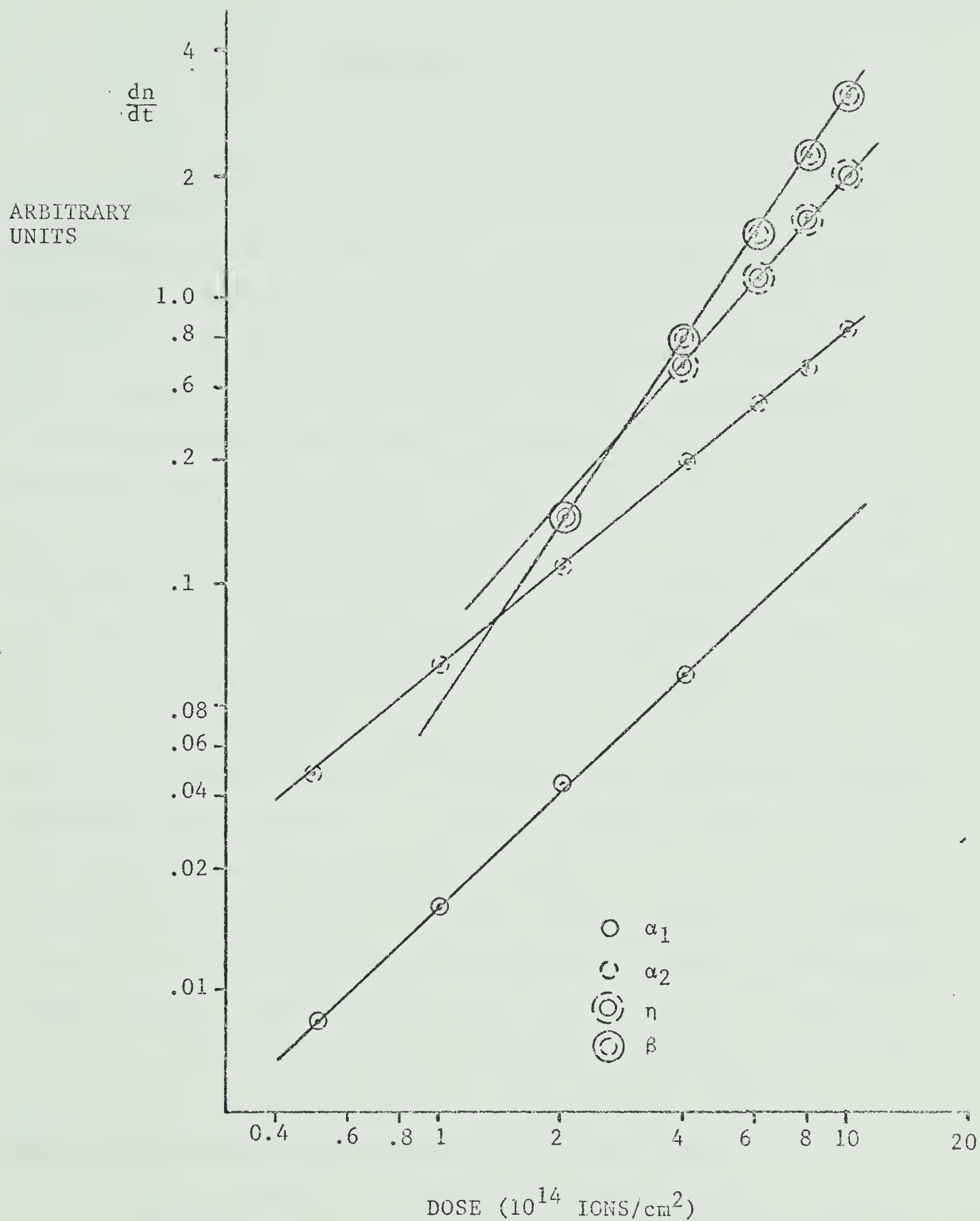


FIGURE 5.13 DESORPTION RATE AS A FUNCTION OF DOSE
(LOGARITHMIC)

CHAPTER 6

CONCLUSION

The results given in the previous chapter show four modes of gas trapping and desorption in a stainless steel sample. Two modes, believed due to interstitial and vacancy migration on the surface occur below a critical bombarding energy, and are therefore considered to be intrinsic to the material tested. The activation energy measured will vary slightly for different gases because of interaction between the trapped gas and normal lattice atoms. The activation energy of the other reactions varied with incident energy and dose. Bombardment induced damage is believed to promote bubble nucleation at the surface or para-surface. The amount of gas trapped in the surface sites began to decrease for bombarding energies approaching 500 eV while the fourth peak, due to diffusion of gas trapped at greater depths, began to increase. This indicates that the collision cross-section of helium began to decrease for incident energies greater than 400 eV. Bombarding ions had fewer collisions with surface atoms and a larger proportion of incident ions were trapped in deeper sites. In addition to being sensitive to incident ion mass, the results obtained may vary due to composition variations amongst samples. Chromium and nickel content in type 304 stainless steel, for example, may vary by 2% and 4% respectively. It is felt, however, that the results obtained give a general indication of trapping and desorption processes in stainless steel.

To this extent, the underlying purpose of the thesis has been accomplished. A UHV system was built and found to meet design specifications. Pressures of 1.5×10^{-10} torr or less were achieved, and its versatility has been demonstrated to some degree by the manner

in which unexpected difficulties were easily overcome.

Additional tests should be conducted with various inert gases and possibly several different target materials. In order to carry out these experiments, it may be necessary to vary the time constant of the differentiator and the heating rate of the sample. An automatic temperature function generator with variable heating rates would provide easier and more accurate control of the specimen temperature. Complementary tests such as ion-induced desorption may yield additional information on trapping mechanisms of commonly used vacuum materials.

BIBLIOGRAPHY

1. G.J. Dienes and G.H. Vineyard, Radiation Effects in Solids, Interscience Publishers, 1957.
2. J.D. Eshelby, J. Appl. Phys., 25, pp. 255, 1954
3. C. Kittel, Introduction to Solid State Physics, John Wiley and Sons, New York, London, Sydney, 1967
4. J.M. Burgers, Proc. Phys. Soc. (London), 52, 23, 1940
5. H.B. Huntington and F. Seitz, Phys. Rev., 61, 315, 1942
6. H.D. Hagstrum, Phys. Rev., 104, 317, 1956
7. G. Carter and J.S. Colligen, Ion Bombardment of Solids, American Elsevier Publishing Co., 1968
8. L.H. Van Vlack, Elements of Materials Science, Addison Wesley, 1962
9. P.A. Redhead, Vacuum, 12, 4, pp. 203, 1962
10. G. Carter, Vacuum, 12, 5, pp. 245, 1962
11. E.V. Kornelsen, J. Vac. Sci. Tech., 6, pp. 173, 1969
12. R. Kelly and H.J. Matzke, J. Nucl. Materials, 17, pp. 179, 1965
13. E.V. Kornelsen, J. Appl. Phys., 39, pp. 10, 1968
14. E.V. Kornelsen, F. Brown, J.A. Davies, B. Domeij and G.R. Piercy, Phys. Rev., 136, A849, 1964
15. J.B. Gibson, A.N. Goland, M. Milgram and G.H. Vineyard, Phys. Rev., 120, pp. 1229, 1960
16. B. Jouffrey, Ph.D. thesis, University of Paris, 1964
17. R. Bayley, Ph.D. thesis, University of Salford
18. R.S. Barnes and D.J. Mazey, Proc. Roy. Soc., 47, pp. 275, 1963
19. J.H.O. Varley, Phil. Mag., 7, pp. 301, 1962
20. R.O. Rantanen, A.L. Moen and E.E. Donaldson, J. Vac. Sci. and Tech., 7, 1, pp. 18
21. P.G. Lucasson and R.M. Walker, Phys. Rev., 127, 485, pp. 1130, 1962
22. C.E. Birchenall and R.F. Melh, J. Appl. Phys., 19, 217, 1964
23. R. Borg and E. Birchenall, Trans. AIME, 218, 980, 1960
24. J.F. Truhlar, E.E. Donaldson, and D.E. Horne, J. Appl. Phys., 41, 5, pp. 2139

25. D.W. Barrett, Proc. Roy. Soc., A236, 1965
26. K. Erents and G. Carter, Vacuum, 16, 10, pp. 523

B29988